MODIFICATION OF MORPHOLOGICAL AND WETTING PROPERTIES OF NANOCRYSTALLINE $FeSi_2$ AND Fe_3Si FILMS THROUGH PLASMA ETCHING

NATTAKORN BORWORNPORNMETEE

A THESIS SUBMITTED IN PARTIAL FULFILLMENT OF THE REQUIREMENT FOR THE DEGREE OF MASTER OF SCIENCE IN APPLIED PHYSICS

DEPARTMENT OF PHYSICS SCHOOL OF SCIENCE
KING MONGKUT'S INSTITUTE OF TECHNOLOGY LADKRABANG

2022
KMITL-2022-SC-M-030-092

COPYRIGHT 2022
SCHOOL OF SCIENCE
KING MONGKUT'S INSTITUTE OF TECHNOLOGY LADKRABANG

Thesis Title	Modification of Morphological and Wetting Properties of Nanocrystalline $FeSi_2$ and Fe_3Si Films through Plasma Etching
Student Name	Mr. Nattakorn Borwornpornmetee
Student ID	62605035
Degree	Master of Science (Applied Physics)
Department	Physics
Year	2022
Thesis Advisor	Asst. Prof. Dr. Nathaporn Promros

Abstract

This research was regarding nanocrystalline $FeSi_2$ films and Fe_3Si films that were epitaxially formed on Si(111) wafers via facing-targets direct-current sputtering at a room temperature and substrate temperature of 300°C, respectively. Both films were divided and etched by Ar plasma at different power of 50, 100, and 150 W. From the scanning electron microscopy and atomic force microscope images, the surface morphology of the as-created nanocrystalline $FeSi_2$ films showed numerous small uniform crystallites and roughness of 1.04 Å. The surface for all etched nanocrystalline $FeSi_2$ films showed appearance of hole and increase in roughness. The Fe_3Si samples also share similar trait. XPS result showed that films cover by carbon which was a source of hydrophobicity. After etching, the content of carbon decrease and oxide presence increase on both films as the power increased. The average contact angle of the unetched nanocrystalline $FeSi_2$ film surface was 100.55°, which is hydrophobic. The nanocrystalline $FeSi_2$ film surface reached a minimum contact angle of 35.65°, which belong to hydrophilic state, when the etching power was increased to 150 W. The average contact angle for the surface of the as-created Fe_3Si films possessed a contact angle of 101.70°. Fe_3Si also shift from hydrophobic to hydrophilic after etching. The contact angle decreased to 67.05° at an etching power of 150 W. The mechanical properties of both films rarely affect by Ar plasma.

Keywords : Argon Plasma, Plasma etching, Nanocrystalline $FeSi_2$, Fe_3Si, Wettability

Acknowledgements

I am sincerely grateful to my advisor, Asst.Prof.Dr. Nathaporn Promros, for all of his help, counsel, and compassion to myself and the other research members. While studying at King Mongkut Institute of Technology Ladkrabang (KMITL), Asst.Prof.Dr. Nathaporn Promros constantly gives me opportunity to develop my talents.

I would like to convey my heartfelt appreciations to Dr. Mati Horprathum, the chairperson, for his assistance and excellent research recommendations in improving the quality of our study. It was a privilege to have his assistance, both at KMITL and the National Electronics and Computer Technology Center (NECTEC).

I would like to express my gratitude to Asst.Prof.Dr. Pisan Sukwisute, the honorable examiner, and the talented lecturers of the Department of Physics at KMITL for their invaluable research and study advise, which they constantly provide to all of their students.

I would like to recognize Prof. Dr. Tsuyoshi Yoshitake and his research student for all of their advise and research assistance in a variety of ways.

Furthermore, I would like to appreciate the help that Mr. Peerasil Charoenyuenyao and Ms. Rawiwan Chaleawpong, including Mr. Phongsaphak Sittimart bestowed to me during my research.

At last, I would like to give all my thankfulness to my parents for their support and encouragement in many kinds.

Mr. Nattakorn Borwornpornmetee

Table of Contents

Page

Abstract in English i
Acknowledgements ii
Table of Contents iii
List of Tables vii
List of Figures viii
Chapter 1 Introduction 1
1.1 Research motivation 1
1.2 Objectives of the study 2
1.3 Scopes of the study 3
1.4 Research organization 3
1.5 Benefits of the study 3
Chapter 2 Theory and Literature Reviews 4
2.1 Physical features of nanocrystalline $FeSi_2$ 4
2.2 Physical features of Fe_3Si 6
2.3 Deposition method 8
2.3.1 Facing-target direct-current sputtering (FTDCS) 8
2.4 Plasma etching 9
2.4.1 Conventional set up for plasma procedure 10
2.4.2 Mechanism behind the plasma etching 11
2.5 Wettability of surface 12
2.5.1 Contact angle 13
2.5.1 Wetting model of Wenzel and Cassie-Baxter 14
2.6 Characterization methods 16
2.6.1 X-ray diffraction (XRD) 16
2.6.2 X-ray photoelectron spectroscopy (XPS) 17
2.6.3 Scanning electron microscope (SEM) 18
2.6.4 Atomic force microscopy (AFM) 18
2.6.5 Contact angle measurement 19
2.6.6 Nanoindentation 20

Table of Contents (cont.)

2.7 Related research 21
2.7.1 Impact of argon plasma exposure on the material's properties 21
2.7.2 Studies on effect of plasma power on the material's properties 22
Chapter 3 Research methodology 25
3.1 Creation of nanocrystalline $FeSi_2$ and Fe_3Si films 25
3.1.1 Production of nanocrystalline $FeSi_2$ on Si(111) wafer substrates 26
3.1.2 Production of Fe_3Si on Si(111) wafer substrates 27
3.2 Plasma etching apparatus 28
3.2.1 Preparation of samples for Etching 29
3.3 Etching process 30
3.3.1 Etching procedure 30
3.3.2 Etching condition 32
3.4 Characterization of the properties of unetched and etched films 33
3.4.1 Structure of films 33
3.4.2 Surface composition of films 34
3.4.3 Surface morphology of films 34
3.4.4 Surface roughness of the films 35
3.4.5 Contact angle measurement 36
3.4.6 Mechanical investigation 37
Chapter 4 Results and Discussion 38
4.1 Physical properties of as-produced nanocrystalline $FeSi_2$ films 38
4.1.1 XRD pattern of as-produced nanocrystalline $FeSi_2$ films 38
4.1.2 XPS spectrum of as-produced nanocrystalline $FeSi_2$ films 39
4.1.3 FESEM image of as-produced nanocrystalline $FeSi_2$ films 40
4.1.4 AFM image of as-produced nanocrystalline $FeSi_2$ films 41
4.1.5 Wettability of as-produced nanocrystalline $FeSi_2$ films 42

Table of Contents (cont.)

4.1.6 Mechanical property of as-produced nanocrystalline $FeSi_2$ films 42
4.2 Physical properties of unetched and etched nanocrystalline $FeSi_2$ films 44
4.2.1 XRD patterns of unetched and etched nanocrystalline $FeSi_2$ films 44
4.2.2 XPS spectra of the unetched and etched nanocrystalline $FeSi_2$ films 45
4.2.3 FESEM of unetched and etched nanocrystalline $FeSi_2$ films .. 46
4.2.4 AFM images of unetched and etched nanocrystalline $FeSi_2$ films 47
4.2.5 Wettability of unetched and etched nanocrystalline $FeSi_2$ film surface 48
4.2.6 Mechanical property of unetched and etched nanocrystalline $FeSi_2$ film surface 50
4.3 Physical properties of as-produced Fe_3Si films 51
4.3.1 XRD pattern of as-produced Fe_3Si films 52
4.3.2 XPS spectrum of as-produced Fe_3Si films 51
4.3.3 FESEM image of as-produced Fe_3Si films 53
4.3.4 AFM image of as-produced Fe_3Si films 54
4.3.5 Wettability of as-produced Fe_3Si films 54
4.3.6 Mechanical property of as-produced Fe_3Si films 55
4.4 Physical properties of unetched and etched Fe_3Si films 56
4.4.1 XRD patterns of unetched and etched Fe_3Si films 56
4.4.2 XPS spectra of the unetched and etched Fe_3Si films 57
4.4.3 FESEM images of the unetched and etched Fe_3Si films 58
4.4.4 AFM images of unetched and etched Fe_3Si films 60
4.4.5 Wettability of unetched and etched Fe_3Si films 61
4.4.6 Mechanical property of unetched and etched Fe_3Si films 62

Table of Contents (cont.)

Chapter 5 Summary and Suggestions for Future Work 65
5.1 Summary 65
5.2 Suggestions 66
References 67
Appendix/Appendices 75
Appendix A 76
Author Biography 78

List of Tables

Table **Page**

1.1 Research procedures 3

2.1 The root mean square (rms) value of AZO film was treated by argon plasma at different operating pressure and plasma power 24

3.1 Conditions for the creation of nanocrystalline $FeSi_2$ films 26

3.2 Conditions for the creation of Fe_3Si films 27

3.3 List for components of plasma apparatus control panel. 29

3.4 etching conditions for the nanocrystalline $FeSi_2$ and Fe_3Si films 32

4.1 Atomic concentration of nanocrystalline $FeSi_2$ films created by FTDCS. 40

4.2 H and E_r for unetched nanocrystalline $FeSi_2$ created by FTDCS in comparison with various materials 43

4.3 Atomic concentration of nanocrystalline $FeSi_2$ films at different MW plasma treatment conditions 46

4.4 H and E_r for unetched nanocrystalline $FeSi_2$ and Ar plasma etched nanocrystalline $FeSi_2$ 51

4.5 Atomic concentration of Fe_3Si films at different MW plasma treatment conditions 52

4.6 H and E_r for unetched Fe_3Si created by FTDCS at 300°C in comparison with various materials 56

4.7 Atomic concentration of Fe_3Si films at different MW plasma etching conditions 58

4.8 H and E_r for unetched Fe_3Si and Ar plasma etched Fe_3Si 64

List of Figures

Figure **Page**

2.1 XRD patterns of nanocrystalline $FeSi_2$ films formed via PLD and FTDCS. The inset of Fig. 2.6 is the micro-area electron diffraction (MD) pattern of the nanocrystalline $FeSi_2$ film produced via PLD 5

2.2 The Dark-field TEM image of the nanocrystalline $FeSi_2$ thin films formed via PLD 6

2.3 (a) Phase diagram of iron silicide where ordered, homogeneous phase regions are indicated by the grey shading. (b) Unit cell of the $D0_3$ structure of Fe3Si made up of bcc and CsCl sub-cubic structure 7

2.4 XRD pattern of Fe3Si expitaxially deposited onto Si(111) via FTDCS by Yoshitake et al 8

2.5 The schematic diagram of the FTDCS system 9

2.6 Schematic of Microwave etcher 11

2.7 Variation of plasma interaction 11

2.8 Illustration of contact angles on a smooth surface of substrate 13

2.9 The illustration of the liquid shape on the smooth surface substrate in different range of contact angle 13

2.10 Illustration of contact line for liquid on a flat surface 14

2.11 Illustration of (a) Wenzel interface and (b) Cassie-Baxter interface 14

2.12 Diagram for XRD method 16

2.13 Principal schematic of the XPS device 17

2.14 2D-diagram for SEM equipment 18

2.15 Basic diagram for AFM equipment 19

2.16 Photograph taken from sessile drop contact angle measurement 20

2.17 Schematic diagram for a nanoindentation apparatus 21

2.18 XPS analysis of titanium and plasma-modified titanium 21

2.19 Contact angle of titanium and plasma-modified titanium 22

2.20 Effect of (a) exposure time and (b) RF power on the contact angles to water of PVC 22

List of Figures (cont.)

Figure **Page**

2.21 SEM surface images PVC at different condition of (a) original PVC, (b) directed argon plasma treated PVC, and (c) remote argon plasma treated PVC at 60 W for3 minutes 23

2.22 XRD patterns of the AZO films were treated at the different (a) operating pressures and (b) plasma power 23

2.23 AFM images of AZO film were treated by argon plasma at the different (a) operating pressure and (b) plasma power..... 24

3.1 FTDCS system for the production of nanocrystalline $FeSi_2$ and Fe_3Si films 25

3.2 Plasma etching apparatus for etching the nanocrystalline $FeSi_2$ and Fe_3Si 28

3.3 The control panel of low-pressure plasma system (Diener electronic, model: Pico) 29

3.4 Images of (a) the sample preparation process and (b) the prepared samples 30

3.5 Images of the cleaned room at Beamline 6a, Synchrotron Light Research Institute, Thailand 30

3.6 The panel of microwave generator (Diener electronic, model: MWG 1200) 31

3.7 Vacuum chamber when opened for sample loading..... 31

3.8 plasma chamber while operating..... 32

3.9 The as-produced and etched nanocrystalline $FeSi_2$ films 33

3.10 The as-produced and etched Fe_3Si films 33

3.11 The XRD diffractometer (Rigaku, TTRAX III) at MTEC 34

3.12 XPS equipment (Kratos Analytical, AXIS Ultra DLD) 34

3.13 The Hitachi SU 8230 FESEM apparatus 35

3.14 AFM apparatus (Park system, XE-120) 35

3.15 Contact angle analyzer (OCA 20) and a display monitor 36

3.16 Drop on the surface of films in (a) normal view and (b) view on the monitor with an estimation of contact angle values..... 36

3.17 Nanoindentation apparatus (Micromaterial, model Nanotest Vantage)..... 37

4.1 XRD patterns at a fixed incidence angle of 2° of the as-produced nanocrystalline $FeSi_2$ films formed by means of FTDCS 39

List of Figures (cont.)

Figure **Page**

4.2 XPS lines of as-created nanocrystalline $FeSi_2$ films produced by FTDCS..... 40

4.3 FESEM surface of the produced nanocrystalline $FeSi_2$ layer formed via FTDCS 41

4.4 Illustration of AFM for the surface of unetched nanocrystalline $FeSi_2$ films 41

4.5 Image of water droplet on the surface of the nanocrystalline $FeSi_2$ films 42

4.6 Load-depth plots of the nanocrystalline $FeSi_2$ films created by FTDCS 43

4.7 XRD spectra for nanocrystalline $FeSi_2$ films without etching and etching at different plasma power 44

4.8 XPS spectra of etched nanocrystalline $FeSi_2$ films under various etching power in comparison with as-produced nanocrystalline $FeSi_2$ films..... 45

4.9 Plain-view FESEM micrographs for the as-produced nanocrystalline $FeSi_2$ films at and after etching at 50 W, 100 W, and 150 W 47

4.10 AFM images of the nanocrystalline $FeSi_2$ films in the case of unetched and etched under various power of 50, 100, and 150 W..... 48

4.11 Images of contact angles for the as-produced nanocrystalline $FeSi_2$ films and nanocrystalline $FeSi_2$ films etched at 50, 100, and 150 W 49

4.12 Load-depth plots of the nanocrystalline $FeSi_2$ films etched at 50, 100, and 150 W..... 50

4.13 XRD patterns of the as-produced Fe_3Si films formed by means of FTDCS..... 51

4.14 XPS spectra of unetched Fe_3Si films formed by means of FTDCS 52

4.15 FESEM (a) surface and (b) cross-section of the produced Fe_3Si layer formed via FTDCS 53

4.16 Illustration of AFM for the surface of unetched Fe_3Si films 54

4.17 Image of water droplet on the surface of the Fe_3Si films 55

4.18 Load-depth plots of the Fe_3Si films created by FTDCS at 300°C 55

4.19 XRD patterns of the as-produced and etched Fe_3Si films 57

4.20 XPS spectra of etched Fe_3Si films under various etching powers in comparison with as-produced Fe_3Si films 58

List of Figures (cont.)

Figure **Page**

4.21 FESEM images in plane surface view of as-created Fe_3Si films and after etching at powers of 50 W, 100 W, and 150 W 59

4.22 Crossectional view of as-created Fe_3Si films and after etching at powers of 50 W, 100 W, and 150 W. 60

4.23 AFM images of the Fe_3Si film surfaces in case of unetched and etched at power of 50, 100, and 150 W 61

4.24 Contact angles of (a) as-produced and etched Fe_3Si films at (b) 50, (c) 100, and (c) 150 W 62

4.25 Load-depth plots of the as-created Fe_3Si films and the films after etching at 50, 100, and 150 W 63

S1 The (a) VSM plot between mass magnetization versus applied magnetic field and (b) hysteresis loop of the etched and unetched Fe_3Si film's surface 76

S2 The separated hysteresis loop based on plot between ratio of mass magnetization and saturated magnetization versus applied magnetic field of (a) unetched, (b) 50 W, (c) 100 W and (d) 150 W treated Fe_3Si film. 77

Chapter 1
Introduction

1.1 Research motivation

Fe-Si compounds were created from elements that are environmentally friendly and non-toxic elements that are abundant natural resources [1,2]. Ferromagnetic iron disilicide (Fe_3Si) has a slight lattice mismatch of +4.2% with semiconducting Si and of -2.5% with the semiconductor phase of the iron disilicide ($FeSi_2$) compound has an orthorhombic (β) structure (β-$FeSi_2$) [3,4]. Fe_3Si has a high Curie temperature of 840 K. Further, it has a cubic DO_3 structure and can be regarded as a Heusler alloy: Fe_2FeSi [4,5]. Fe_3Si also possesses good hardness and resistance to corrosion [6]. The β-$FeSi_2$ films that possesses desirable characteristics. Its absorption coefficient value is over 10^5 cm^{-1} for the photons with an energy range that exceeds 1.2 eV, and it has an 0.76 eV indirect bandgap as well as an 0.85 eV direct bandgap for the optical transition [7-9]. Both of these are in adherence to the wavelength for optical telecommunications ranging from 1.3 to 1.5 microns [7,8]. Nanocrystalline $FeSi_2$ with a crystalline size of less than 10 nm in diameter holds unique characteristics like those of β-$FeSi_2$ [9-11]. Its optical band gap value is mostly identical to that of β-$FeSi_2$, while its absorption coefficient value is greater than that of β-$FeSi_2$ [11]. Furthermore, it was observed that nanocrystalline $FeSi_2$ and Fe_3Si films could be grown on to a wide array of substrates [4,11]. They also possess an extremely smooth surface. Based on these properties, nanocrystalline $FeSi_2$ and Fe_3Si is a potential candidate for use as a hydrophobic coating material.

Even though there have already been several reports on the application of nanocrystalline $FeSi_2$ films to NIR photodiodes and Fe_3Si as magnetic materials, the investigations concerning other applications, such as hydrophobic surfaces and hard coating based on these films, have been neglected [3,9]. In the previous research, the wetting characteristics of the nanocrystalline $FeSi_2$ constructed via sputtering were studied. It was found that the nanocrystalline $FeSi_2$ film surface is hydrophobic, as the contact angle between the water droplet and the film surface was above 90° [12]. Additionally, the variations for the contact angle, including the structural and morphological characteristics after the thermal annealing procedure, were revealed

[13,14]. However, thermal annealing had proved to be ineffective in this regard. Hence, a new method to modify the wetting property of materials based on Fe-Si is needed. Numerous researchers have reported that the physical characteristics of the films can be altered via the usage of a plasma etching procedure [15-21]. Plasma etching is a procedure that modifies the material's surface led to a change in roughness [15,16]. More importantly, plasma ion can reactively interact with the surface and remove some particle or contaminant from it which enhances the properties and quality of materials [17-21]. Among the conventional plasma, argon plasma possesses a set of intriguing characteristics [15-21]. Argon plasma treatment roughens the surface of the material and could also prevent oxidation of the surface as the plasma breaks the oxygen bond with the metal surface [21]. Enthrallingly, it has been reported that argon plasma could shift the wetting state of the material from hydrophobic to hydrophilic [17]. Based on the information above, argon plasma etching might be able to unlock a new possibility within the nanocrystalline $FeSi_2$ films and by extension Fe_3Si films.

For these reasons, this work will be focused on the modification of the wettability and surface morphology properties of the nanocrystalline $FeSi_2$ and Fe_3Si films. The experimental findings of this work are relevant to the impacts of argon plasma etching on the morphological and wettability properties of nanocrystalline $FeSi_2$ and Fe_3Si films. The argon plasma etching power will be altered for the optimization of the wettability and morphological characteristics. It is expected that the changes in microwave etching power will modify the roughness of the nanocrystalline $FeSi_2$ and Fe_3Si film surface, which may lead to the modification of the contact angle of the nanocrystalline $FeSi_2$ and Fe_3Si films surface and could open another route for their development as self-cleaning surface.

1.2 Objectives of the study

1) To create and modify surface of nanocrystalline $FeSi_2$ an Fe_3Si films using microwave plasma under argon atmosphere.
2) To study the effect of plasma etching on morphological and wetting properties of the nanocrystalline $FeSi_2$ and Fe_3Si films.

1.3 Scopes of the study

1) nanocrystalline $FeSi_2$ and Fe_3Si films were created through facing-target direct-current sputtering.
2) nanocrystalline $FeSi_2$ and Fe_3Si films were etched by argon plasma at different microwave power of 50, 100, and 150 Watts.
3) The investigation on the surface morphology and wettability of the nanocrystalline $FeSi_2$ and Fe_3Si films in the case of unetched and etched under various microwave power were executed.

1.4 Research organization

Table 1.1 Research procedures

Procedure	Period								
	Jul	Sep	Oct	Nov	Dec	Jan	Feb	Mar	Apr
Study the article corresponding to the research topic	←	—	—	—	—	→			
Investigate the surface morphology and wettability of the as-deposited films	←	—	—	—	—	→			
Etched the as-deposited films with microwave argon plasma			←	—	—	→			
Characterize the surface morphology and wettability of the etched films					←	—	—	→	
Organize the topic for each chapter and write down the thesis					←	—	—	—	→

1.5 Benefits of the study

1) Surface morphology and wettability of as-deposited nanocrystalline $FeSi_2$ and Fe_3Si films were reported.
2) Surface morphology and wettability of nanocrystalline $FeSi_2$ and Fe_3Si films were altered after etched at different microwave power by argon plasma.
3) Effects of argon plasma on surface morphology and wettability of nanocrystalline $FeSi_2$ and Fe_3Si films were demonstrated.

Chapter 2
Theory and Literature Reviews

This chapter reviews the essential background for discussing the physical properties of Fe-Si based materials as well as the basic concepts of wettability properties. It starts with a discussion of the semiconducting properties of nanocrystalline $FeSi_2$ and FeSi are then discussed. Next, the backgrounds of the deposition method, wettability, and plasma etching are described. Previously published papers related to this study are discussed and compared with the current research.

2.1. Physical features of nanocrystalline $FeSi_2$ [22-37]

A previous report was made by M. Milosavlijevic et al. concerning the discovery of an amorphous form of $FeSi_2$. Through ion-beam mixing (IEM) of Fe layers, homogenous amorphous $FeSi_2$ layer was produced onto Si at 300 °C utilizing Ar^{8+} ions. The measurements of optical absorption revealed a direct band gap of around 0.88 eV. The formation of amorphous $FeSi_2$ was credited to the swift Si diffusion onto the surface. Previously, nanocrystalline $FeSi_2$ films were successfully created via PLD employing $FeSi_2$ targets, after which their physical properties were investigated. In recent years, nanocrystalline $FeSi_2$ has become a promising candidate for use in near-infrared (NIR) semiconductors and coating materials. Its physical properties are close to properties possessed by ß-$FeSi_2$ as well as amorphous $FeSi_2$. Further, it is comprised of elements of Fe and Si that are plentiful on earth and environmentally friendly. It is a semiconductor that possesses an optical band gap of 0.87 eV and its absorption coefficient is found to be more than 10^5 cm^{-1} at 1.2 eV. Notably, nanocrystalline $FeSi_2$ films can be created on a variety of substrates that are made of various types of solids at room temperature. In previous research, structure of nanocrystalline $FeSi_2$ films produced by means of PLD and FTDCS were examined by usage of X-ray diffraction (XRD) and TEM. Figure 2.1 depicts the XRD patterns for the nanocrystalline $FeSi_2$ films produced via PLD and FTDCS. These XRD patterns were measured in the mode of 2θ-scan at a fixed incidence angle of 4°. A broad peak appeared at 2θ between 40° and 50°. This broad peak is likely due to the

nanocrystalline structure of the nanocrystalline $FeSi_2$ films. Basically, ß-$FeSi_2$ has many crystalline planes for diffraction, such as 422, 511, 313, 331, 004, 040, 114, and 133, at 2θ between 40° and 50°. The broad peak might be resultant from the overlapping of the diffractions from these crystalline planes. The peak intensity for the nanocrystalline $FeSi_2$ films created via FTDCS was slightly enhanced compared to that of nanocrystalline $FeSi_2$ films produced by means of PLD. This suggests that the crystallite diameters of the nanocrystalline $FeSi_2$ films created via FTDCS are slightly larger than those of the nanocrystalline $FeSi_2$ films produced through PLD. The pattern of micro-area electron diffraction (MD) for the nanocrystalline $FeSi_2$ films produced via PLD demonstrates the weak and broad ring, as depicted in the inset of Figure 2.6. radius of MD result corresponds to the 2.03 Å lattice spacing, which consisted with a weak and broad peak was found at 2θ between 40° and 50° acquired from XRD result. Figure 2.2 presents a dark-field image for the nanocrystalline $FeSi_2$ film produced via PLD using the broad ring. The nanocrystalline $FeSi_2$ films produced through PLD are comprised of many crystallites with diameters between 3-5 nm. This might be a nanocrystalline of ß-$FeSi_2$.

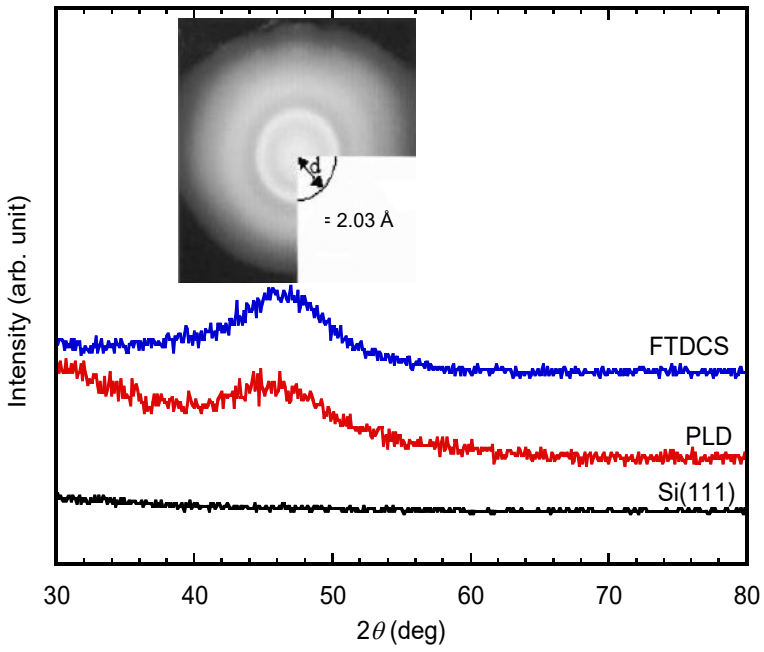

Figure 2.1 XRD patterns of nanocrystalline $FeSi_2$ films formed via PLD and FTDCS. The inset of Fig. 2.6 is the micro-area electron diffraction (MD) pattern of the nanocrystalline $FeSi_2$ film produced via PLD [32].

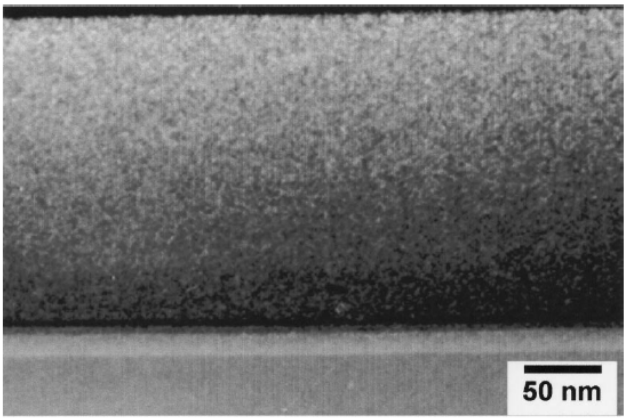

Figure 2.2 The Dark-field TEM image of the nanocrystalline $FeSi_2$ thin films formed via PLD [32].

2.2 Physical features of Fe_3Si [38-42]

Among homogeneous iron silicide phases of different stoichiometry, Fe_3Si is the sole phase of iron-rich composition with well-ordered as shown in Figure. 2.3. It belongs in the bulk phase diagram at room temperature and is steady from there up to the melting point with crystal structure is of $D0_3$ type and can be treated as a Heusler alloy: Fe_2FeSi. Due to Fe and Si randomly occupy the C sites while retain its symmetric structure, silicon atoms in this phase have maximized their mutual distance and dominate an impressively large chunk of the phase diagram from the ideal Si concentration of 25% and below. When Fe or Si randomly occupy C and B sites, The B_2 (CsCl) phase will replace DO_3 phase when Si concentration is below about 10%. At even lower Si composition, Fe or Si will randomly occupy all atomic sites and the A_2 (bcc) phase emerge. At the phase above the idyllic concentration of the $D0_3$ structure, Fe_3Si undergo an sudden transition into an inhomogeneous phase, where its phase boundary ranges from 26% to 31% at room temperature to 1200 °C.

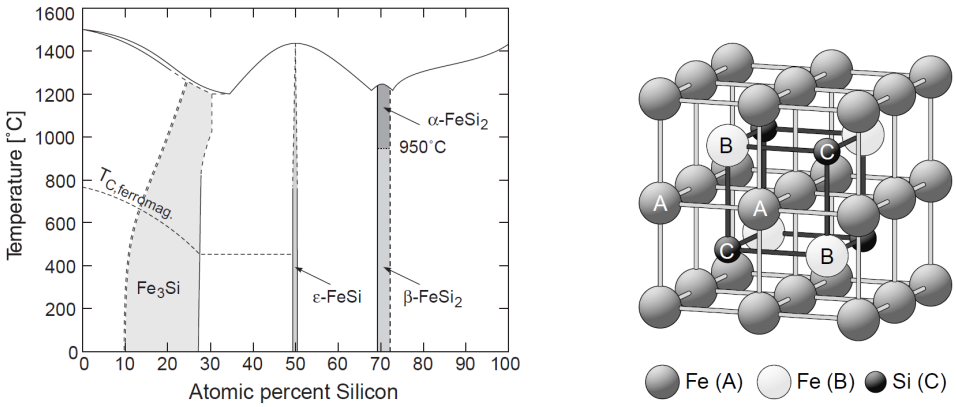

Figure. 2.3 (a) Phase diagram of iron silicide where ordered, homogeneous phase regions are indicated by the grey shading. (b) Unit cell of the $D0_3$ structure of Fe3Si made up of bcc and CsCl sub-cubic structure [38].

Fe-Si alloys have captivated extensive attention for technological and fundamental reasons. Naturally, iron-rich composition displays ferromagnetism, which immediately made it promising candidate as magnetic devices in silicon-based semiconductor device. The ferromagnetic layer offering new potentials abilities to inject and control electric spin in a semiconducting layer to semiconductor device. Ferromagnetic iron silicide or Fe_3Si has lattice constant a=5.653 Å, which is almost the same as that for GaAs. Its lattice constant also slightly mismatch with lattice of semiconducting Si by +4.2% and high Curie temperature of 840 K. At the Fermi stage, the low polarization threshold and high spin polarization is predicted, and it is an attractive electrical spin injection material. Hypothetically, Fe_3Si with a different order of Si atom arrangement, such as B_2 structure, can also have similar properties with DO_3 one. The efficiency of electrical spin injection from a ferromagnet to a semiconductor is highly dependent on their interface quality. To prevent the interdiffusion between the Fe_3Si and the Si layers as a result of the generation of high velocity Fe species, low-temperature growth of this material is needed. Yoshitake et al. [4] reported on the method of epitaxially creating ferromagnetic Fe_3Si films via facing target direct-current sputtering (FTDCS) at room temperature onto Si(111) substrate. This method allowed them to create Fe_3Si films at a low-pressure sputtering and a low deposition rate with precise control. In exchange, the films created this way possess B_2 structure instead of DO_3. This evidenced by from

superlattice reflection appear as (222) orientation XRD pattern, where h, k, and l are all odd number (see Figure 2.4). Therefore T. Sadoh et.al. [5] and K. Hamaya et. al. [40] studied epitaxial growth of the Fe_3Si on Si using molecular beam epitaxy (MBE) for possibility of higher deposition control precision. They successfully synthesized DO_3 structure films with at low temperature with relatively good interface sharpness and magnetic properties.

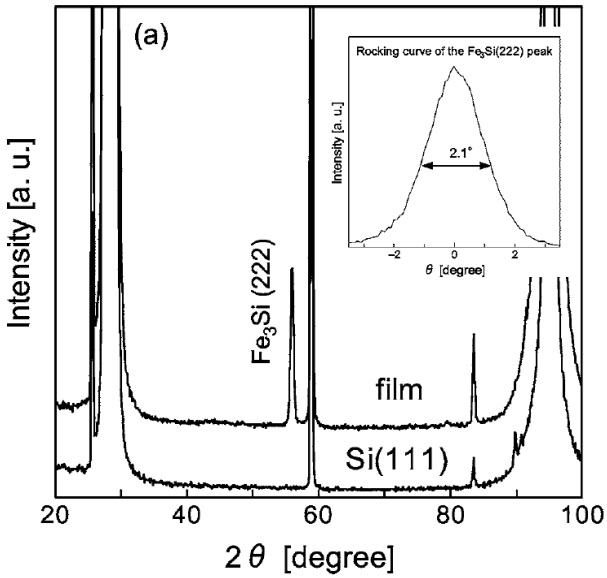

Figure 2.4 XRD pattern of Fe3Si expitaxially deposited onto Si(111) via FTDCS by Yoshitake et al [4].

2.3 Deposition method [43-46]

Sputtering is a physical vapor deposition (PVD) process that is utilized for the growth of thin film layers as well as cleaning and etching of the surface of the film or surface. This process is generated by the bombardment of accelerated ions on the surface of a sputtering target. After the accelerated ions reach the surface of the target with energy above the surface binding energy, a target atom can be ejected from a target and deposited on a substrate.

2.3.1 Facing-target direct-current sputtering (FTDCS)

FTDCS is a modified sputtering system having the advantages of low-substrate temperature and high deposition rate during sputtering. A schematic of the FTDCS system is shown in Figure 2.5. The FTDCS system consists of two circular-

shaped targets with the same dimension. Each target is situated opposing the other. Permanent magnets are arranged in a division behind the pair of targets to form a magnetic field spreading from one target to the other. Such a magnetic field confines plasma, generated by a discharge process, within the discharge area. A sputtering particle formed by the discharge process is deposited on a substrate attached in isolation from the discharge space.

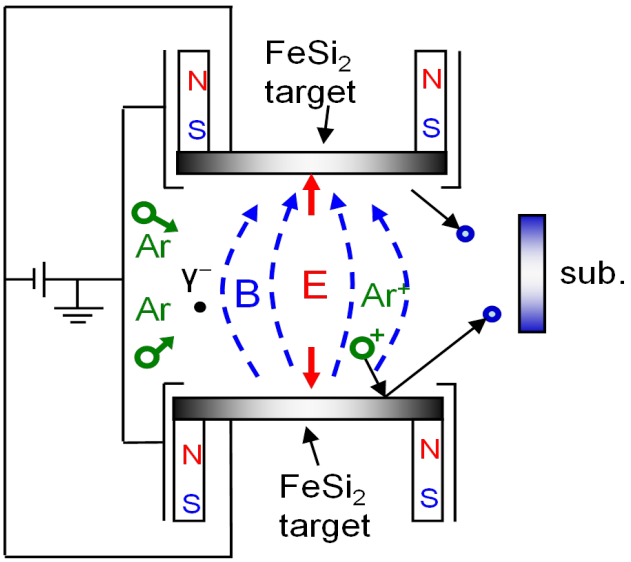

Figure 2.5 The schematic diagram of the FTDCS system.

FTDCS has the following advantages: (i) high plasma density generated from the sputtering process; (ii) sputtering at low pressure operation; (iii) low increment of substrate temperature; (iv) low damage from plasma; and (v) acquired films with low stoichiometric difference comparing to thier target owing to the substrate being free of plasma. Besides, the energy of particles that reach the surface of the substrate is higher when compared to the use of other methods due to sputtering at low pressure.

2.4 Plasma etching [47,48]

A definition of plasma as state within Oxford English dictionary is “An ionized gas consisting of positive ions and free electrons in proportions resulting in more or less no overall electric charge, typically at low pressures (as in the upper atmosphere and in fluorescent lamps) or at very high temperatures (as in stars and nuclear fusion

reactors)". There are two main classifications for plasmas based on the state of thermal equilibrium. First of the two is called hot plasma, whose ions and electrons are close to thermal equilibrium creating fully ionized plasmas. Latter of the two is called cold plasmas which are weakly ionized plasmas due to non-equilibrium generation. In this study, we will solely study on the cold plasma, which were commonly used for plasma etching in the semiconductor industry.

2.4.1 Conventional set up for plasma procedure

Plasma etching chamber have many iterations throughout the years, the more recent one is the microwave excited downstream etcher or microwave etcher, which is widely use due to its versatility. Microwave etcher is the more refined version of normal downstream etcher equipped with microwave source, which mostly operated at 2.45 GHz input. Due to its ability to operate at extremely low pressure (10^{-5} Torr at maximum). The microwave etcher could carry out the etching process that have relatively slow charge-particle recombination in comparison to diffusion and flow while having high plasma density. The microwave etcher offers also better control over the etching process by the subtraction of ions from the plasma area prompted by magnetic field. Contrary to the benefit of ability to easily adjust the condition of the etching process due to being less damaging, the low energy of the ions come with the downside of having lower etching rate. Some of microwave etcher may also equipped with auxiliary magnet coil for even better electron confinement. Schematic of Microwave etcher is presented in Figure 2.6. In this set up, the accelerated energetic charge species within the plasma are charged straight onto the substrate surface and cause the ion bombardment effect. Furthermore, this plasma apparatus can be utilized for material sputtering deposition as well as induce structural and chemical change if flux densities or energy of plasma ion exceed certain level needed for surface bombardment process.

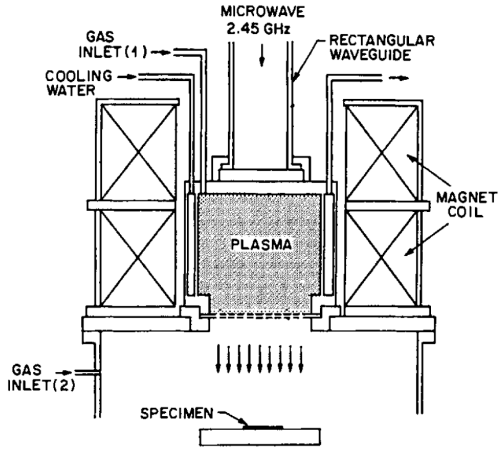

Figure 2.6 Schematic of Microwave etcher [47]

2.4.2 Mechanism behind the plasma etching

Plasma etching can proceed by physical sputtering or chemical reaction and ion-assisted mechanisms. The basic plasma etching processes can be schematically grouped into 3 categories as shown

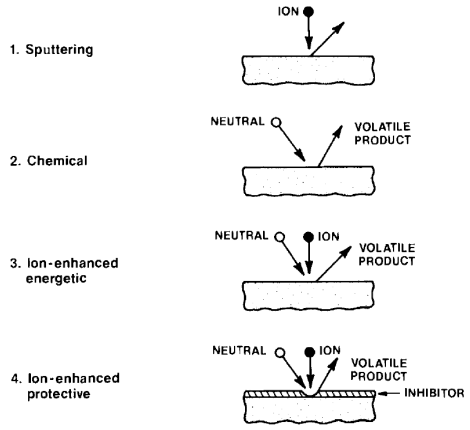

Figure 2.7 Variation of plasma interaction [47]

Plasma etching is a purely physical processes of material removal, where energetic ions transfer impact on the substrate and transfer large amounts of energy and momentum to it and ejected its material. Sputtering etching requires plasma conditions where ion energies are high, existing in low pressure of lower than 50 mTorr. The long mean free paths of low-pressure plasma prevent the reflection and redeposition of the sputtered species when collisions in the gas phase happening. Also, the long mean free paths allow ejected sputtered material to reach opposing

walls across the reactor. However, purely physical method like this requires high energy, resulting in low efficiency, such as low etching rate, surface faceting and trenching as well as electrical damage to the substrate and ion implantation from ion bombardment. In contrast, chemical etching method only relies elementary interaction of gas species a surface. The only requirement of chemical etching process is the formation of a volatile product through chemical reaction. Due to inherently sensitivity to the chemical consistency and variations of bonds, chemical etching is the most selective process of its kind. the occasionally downside of this process is usually its isotropic or nondirectional nature, which vertically and horizontally remove material at the same rate. The fine lines cannot be formed during this removal procedure. When a high energy ion flow contacts with the surface concurrently, energetic ion-enhanced etching causes less ion damage but gains improved reactivity. It creates a quick reaction that forms chemical species and removes material at a pace faster than physical sputtering, causing flaws and dislocations in the lattice or dangling bonds on the surface. A surface compound can occasionally become partially separated. In general, the conventional etching process is based on the transfer of ion energy to the surface, which modifies the surface and makes the impact zone and its surroundings more reactive.

2.5 Wettability of surface [49]

Figure 2.11 presents a liquid drop located on a solid surface. In this case, the contact angle is defined as the angle determined by the intersection of the liquid-solid interface (γ_{sl}), and the liquid-vapor interface (γ_{lv}) (geometrically earned by employing a tangent line from the contact area that closes to the γ_{lv} in the droplet contour). In Figure 2.8, the three phases of the contact line are shown, representing solid, liquid, and vapor. A small contact angle is noticeable when the liquid flattens on the exterior layer of the substrate, while a high contact angle is noted when the liquid forms on the surface in round-shape.

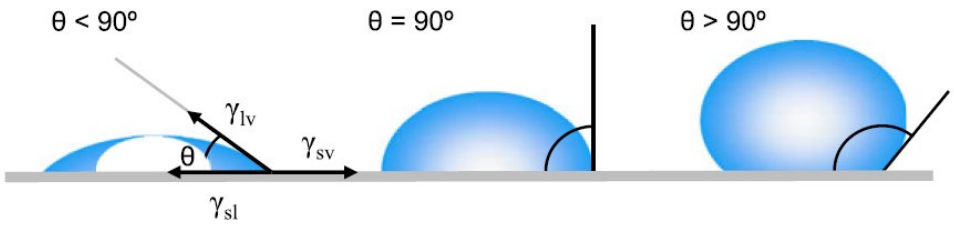

Figure 2.8 Illustration of contact angles on a smooth surface of substrate [47].

The material surface was indicated as a hydrophilic surface where the contact angle values between the drop and contact area of the surface were in a range from 5° to 90°. Namely, the drop will cover a large area on the surface. When the values of contact angle range from 90 to 150°, it can be determined that the surface is hydrophobic. In other words, the contact area between the water droplets is minimal, resulting in maintaining the drop in a sphere. In the case of contact angles evaluated in excess of 150°, the contact surface is shown to have nearly no contact between the drops, called a "Superhydrophobic surface". Conversely, the surface will show superhydrophilic properties where the contact angle values are lower than 5°. In this case, the drop is almost covering the entire contact regime of the substrate surface and showing a flat-shape for the drop on the substrate surface. The wetting behavior of the surface is revealed in Figure 2.9.

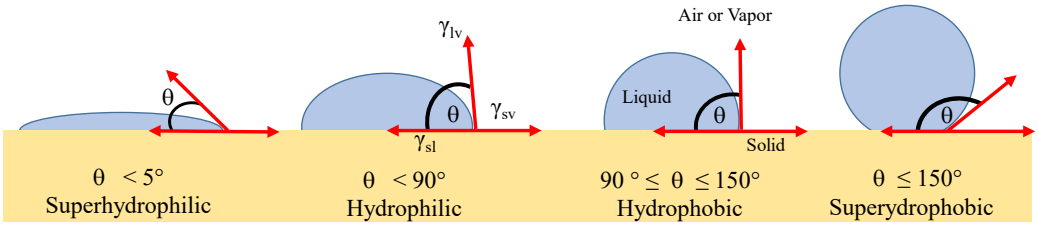

Figure 2.9 The illustration of the liquid shape on the smooth surface substrate in different range of contact angle [47].

2.5.1 Contact angle [50,51]

Atoms on a solid surface possess higher energy due to lack of bonds with its neighboring atoms in comparison to its interior. This surface energy or surface tension (γ) is equal to the work required to produce a unit area of the surface at constant temperature and pressure. As displayed in Figure 2.10, the equilibrium of

the solid surface will be established at a certain angle, when a liquid drop is placed in contact with a solid. This angle called the static contact angle (θ_0), which is given by Young's equation:

$$\cos\theta_0 = \frac{\gamma_{sv} - \gamma_{sl}}{\gamma_{lv}} \qquad (2.1)$$

Where γ_{sv}, γ_{sl} and γ_{lv} are the surface energies of the solid against air, solid against liquid and liquid against air, respectively.

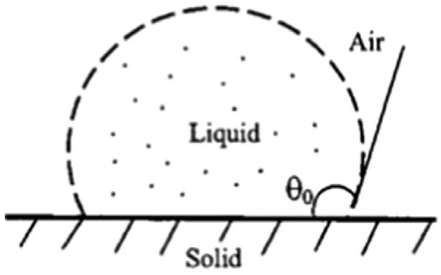

Figure 2.10 Illustration of contact line for liquid on a flat surface [49].

2.5.2 Wetting model of Wenzel and Cassie-Baxter [51-54]

In the case of a rough surface, two wetting models are usually seen: Wenzel's model and Cassie-Baxter's model. These two models are utilized for explanation of the contact angle between the drop and the rough surface, where the drop and air can infiltrate into the groove of the surface. The Wenzel and Cassie-Baxter interface are revealed in Figure 2.11 (a) and (b), respectively.

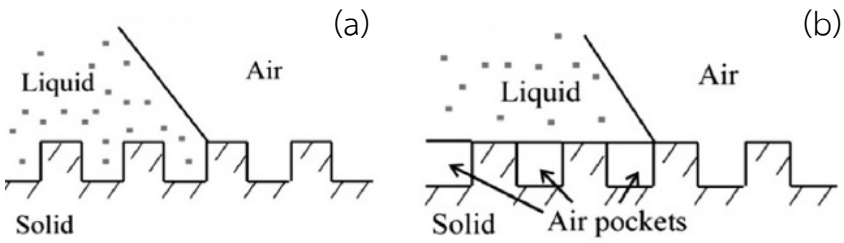

Figure 2.11 Illustration of (a) Wenzel interface and (b) Cassie-Baxter interface [51].

For the Wenzel model, the liquid drops infiltrate into the surface grooves, resulting in higher surface wettability because of the increase in contact area. Wenzel's model describes the contact angle (θ_{CA}) with a rough surface by relating it to that of a flat solid surface. This model modifies Young's equation as follows:

$$\cos\theta_0 = r\left(\frac{\gamma_{sv} - \gamma_{sl}}{\gamma_{lv}}\right) = r\cos\theta \qquad (2.2)$$

Where *r* is the non-dimensional surface roughness factor.

The *r* is defined by the ratio of the actual area of the rough surface to the flat projection area, as symbolized by A_{sl} and A_F, respectively.

$$r = \frac{A_{sl}}{A_F} \qquad (2.3)$$

The Cassie-Baxter model explains that an air pocket occurs underneath the liquid drops, resulting in a larger contact angle. This model assumes a composite surface is comprised of two kinds of patches. The resulting equation is for the apparent contact angle on such a composite surface. Cassie-Baxter's model explains the contact angle with two parameters of fractional area (*f*), and θ_{CA}. The contact angle of this model is given by:

$$\cos\theta = f_1\cos\theta_1 + f_2\cos\theta_2 \qquad (2.4)$$

Where
$$f_1 + f_2 = 1 \qquad (2.5)$$

For composite interface, the first fraction corresponds to the solid–liquid interface, f_{sl} and $\theta_1 = \theta_0$. The second fraction corresponds to the liquid-air interface, $1 - f_{sl}$ and $\theta_2 = 180°$. Combining (2.4) with (2.2), the Cassie-Baxter model can be presented as:

$$\cos\theta = rf_{sl}\cos\theta_0 - 1 + f_{sl} \qquad (2.6)$$

2.6 Characterization methods [55-60]

The basic principle of different characterization techniques used in this research to investigate film's properties is presented this topic.

2.6.1 X-ray diffraction (XRD)

XRD is a technique commonly used for the characterization of crystalline structure. This technique detects the crystal of the coated layer in relation to a single wavelength of an X-ray source. The crystal structure can be categorized as either a monocrystalline or a polycrystalline. Myriad of structural characteristics, such as crystalline structure, crystalline diameter, and atomic spacing can be clarified using XRD. In general, cathode ray tube with a heated filament generates the X-ray, which generate the electron. Under an applied voltage, the generated electrons will proceed to bombard the sample. In case that the incident electrons having a sufficient energy, the electrons from an inner shell would be ejected from the sample and produces an X-ray photons-sample interaction. This results in the Bragg's Law related scattering and absorption as presented below:

$$n\lambda = 2dsin(\theta) \tag{2.7}$$

where n is a diffraction order, λ is a wavelength of the generated X-ray, d is a distance between the atomic layers, and θ is an incident angle.

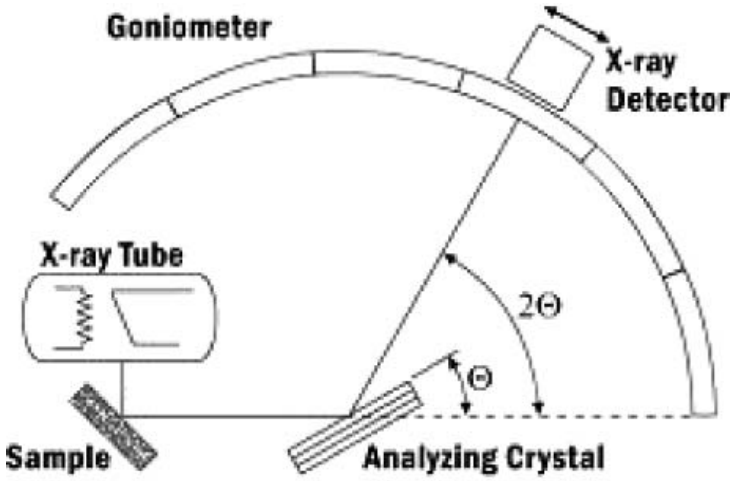

Figure 2.12 Diagram of XRD method. [55]

2.6.2 X-ray photoelectron spectroscopy (XPS)

The XPS technique is one the most powerful methods measuring the chemical composition (both qualitative and quantitative) and bond structure of tested surfaces. At the first step the X-Ray gun generates a directed flow of X-ray with defined energy to the sample surface. A flow of photoelectrons and Auger electrons departed from the sample surface as a result of interaction between an X-Ray beam and tested surface. For the most cases an analysis depth about 1-5 nm can be considered. A loss of kinetic energy due to collisions and scattering occurred for the depth more than 5 nm. Then the ejected photoelectrons focused to the entrance of hemispherical analyzer, where a kinetic energy of photoelectrons can be evaluated. Principal schema of XPS apparatus is shown in Figure 2.13. The XPS spectrum is representing a dependence of counts per unit of time (or intensity) from binding energy (can be recalculated directly from kinetic energy of photoelectrons). Analyzing the peak positions with help of XPS handbooks or XPS spectra databases, a conclusion about chemical elements can be done. Atomic concentrations can be further calculated, bond structure can be analyzed by peak fitting routines.

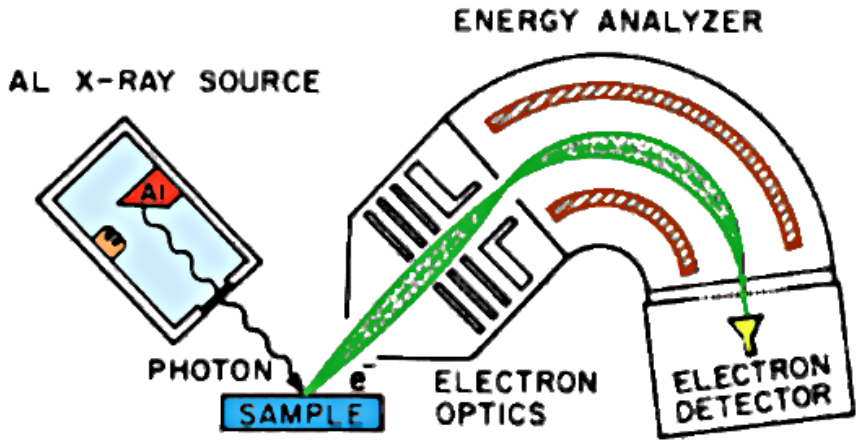

Figure 2.13 Principal schematic of the XPS device. [56]

2.6.3 Scanning electron microscope (SEM)

Figure 2.14 illustrates a 2D-diagram for SEM. SEM is a microscope that employs an electron to hit the atoms of the specimen to create the morphological image of the sample's surface. The backscattered and secondary electrons produce from the source with a sufficient energy had a potential to hit the inner electron of the sample, causing the atom to be excited. Following the excitation of atom, the atom may release Auger electrons or X-ray photons to achieve relaxation process. The electron beam is guides toward the sample through electromagnetic lens. Then, the scanned signal that scatter from the incident electron beam was mapped from each scanning point. Finally, the scanning signal was detected by detector, where the signal will be translated into an image and displayed on the screen.

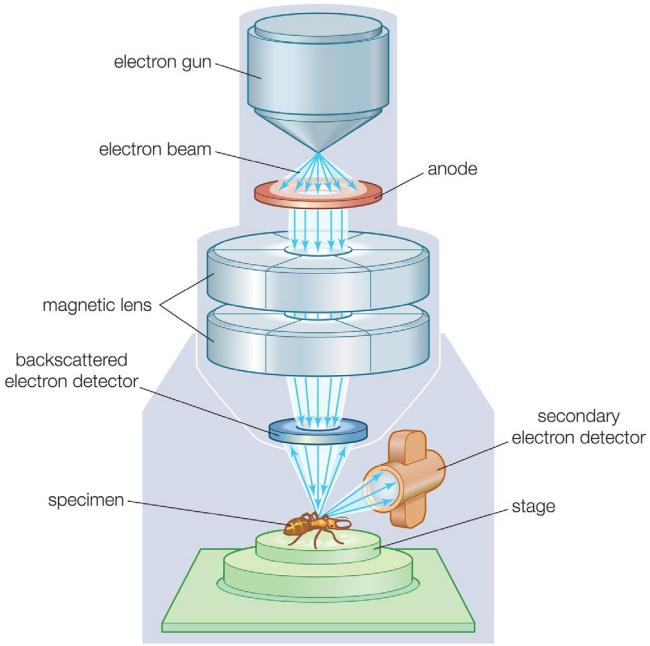

Figure 2.14 2D-diagram for SEM equipment. [57]

2.6.4 Atomic force microscopy (AFM)

An AFM is a nano-resolution microscope which uses a Van der Waals force for an observation of the topological properties of the sample surface. AFM technique can also be used for investigation of mechanical and electrical properties of the sample. The measurement starts by moving a scanning probe over the scanning area. The AFM probe is typically made up of a Si tip and a cantilever set on

a spring with a spring constant smaller than that of the atomic bond. Van der Waals force attracts and repels the scanning probe to the surface. The AFM probe is then pulled down the scanning path, while a laser focused on it is reflected by a reflector on the reverse of the cantilever. The reflected beam is then directed into a photodetector, which tracks the location of the beam to form an AFM picture. A piezoceramic scanner, which is controlled by an electrical feedback loop voltage, maintains the force between the probe's tip and the sample. AFM can be used in contact mode, non-contact mode, or tapping mode.

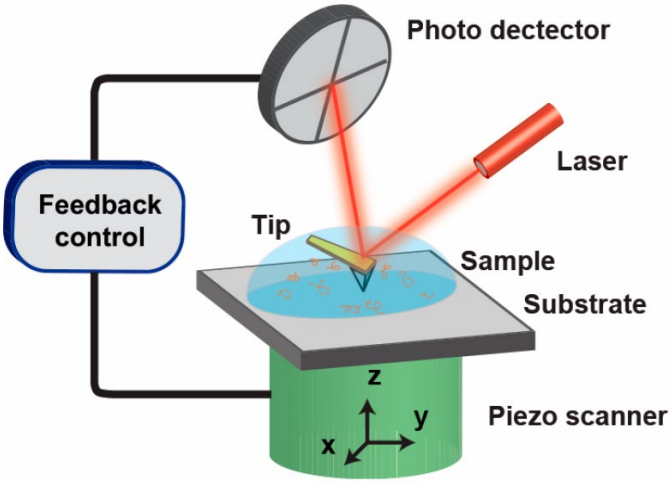

Figure 2.15 Basic diagram for AFM equipment. [58]

2.6.5 Contact angle measurement

Contact angle measurement using a droplet of test liquid such as water, alcohol and oil, including the polar and non-polar liquids to determine a wetting properties of sample surface through a contact angle between the solution and the surface. It can be used for various task such as study of self-cleaning surface, non-stick pans, and waterproof fabrics etc. The contact angle measurement technique that is mostly used is the direct measurement of the static angle of wetting at point of contact known as sessile drop method. These measurements can be taken with various liquids and may be conducted on goniometers. A drop with a well-defined volume is positioned on the sample, and then several photographs are taken and

the angle between the tangent to the drop and the sample is measured for each frame.

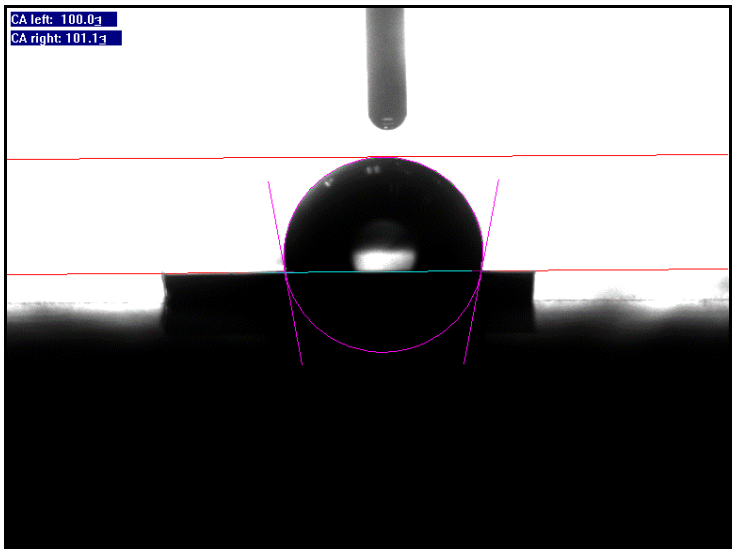

Figure 2.16 Photograph taken from sessile drop contact angle measurement.

2.6.6 Nanoindentation

Nanoindentation is used to study the mechanical properties, such as hardness, stiffness, elasticity, wear resistance and adhesion force of the sample by applying a micro- or nanoscale force on to sample. Figure 2.17 shows the schematic diagram for a nanoindenter. The nanoindentation is performed by the indenter attached to load-controlled instrument. The sample is placed on piezoelectric stage which can be precisely positioning throughout the x-y-z axis. The applied load from a coil and magnet assembly leads the indenter to penetrate the sample's surface under measurement of displacement sensors. The most common indenter is diamond indenter with a three-sided pyramidal geometry called Berkovich tip.

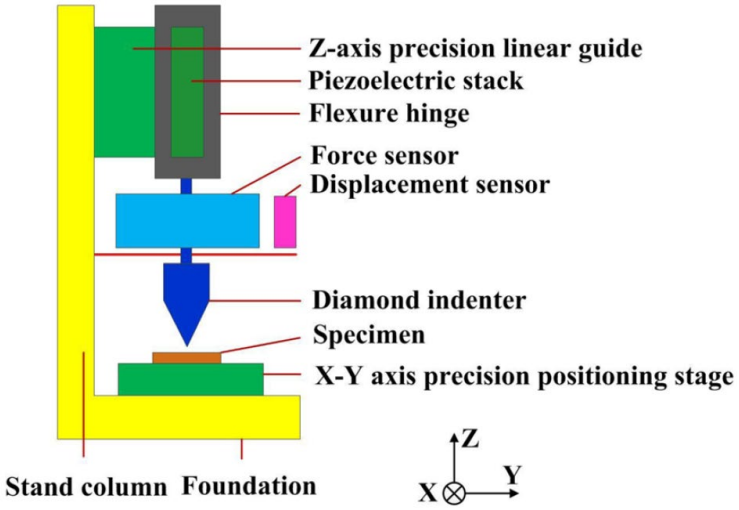

Figure 2.17 Schematic diagram for a nanoindentation apparatus. [60]

2.7 Related research

This section presents the related research of the effect of Etching on films properties from other research groups.

2.7.1 Impact of argon plasma exposure on the material's properties [16]

D. Ujino et.al. reported the effect of plasma treatment of titanium surface employing Ar plasma. After plasma treatment, surface of the Ti films did not undergo the noteworthy change on the morphological properties. On the other hands, surface composition of Ti films changed. The content of oxygen increased, while content of carbon decreased. The changes on composition also reduce contact angle of the films.

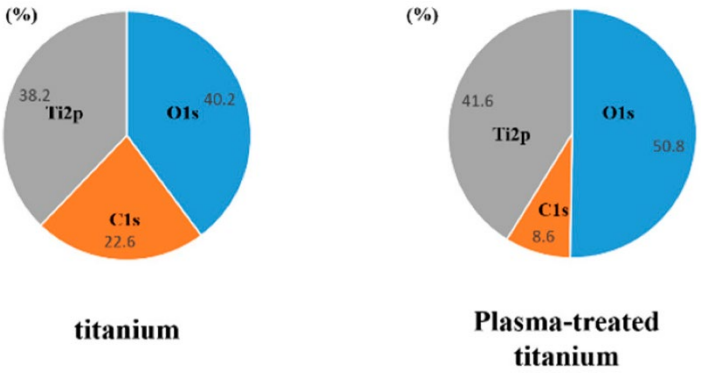

Figure 2.18 XPS analysis of titanium and plasma-modified titanium [16].

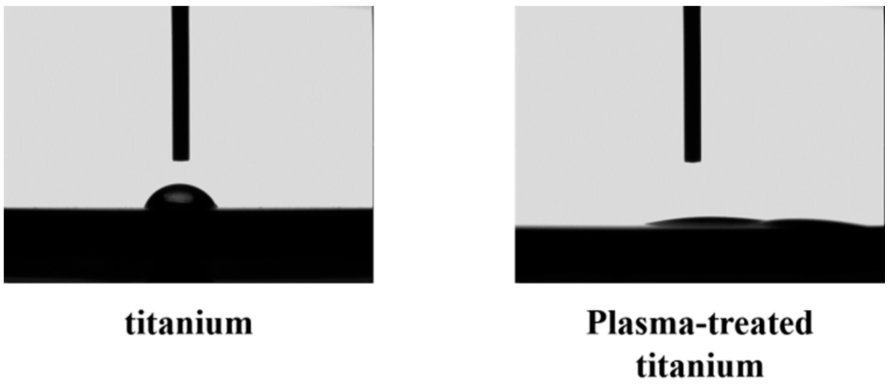

Figure 2.19 Contact angle of titanium and plasma-modified titanium [16].

2.7.2 Studies on effect of plasma power on the material's properties [21,61]

L. Ru and C. Jie-rong studies modification of polyvinyl chloride (PVC) for medical purpose using remote argon plasma treatment. They characterized surface structure and wettability of treated PVC. The results show that the remote argon plasma makes the surface of the PVC film became increasingly hydrophilic as radio frequency (RF) power and the plasma exposure time increased. The wettability of PVC films to be depending on the chemical composition of the sample. In term of physical change, remote plasma posted no treat of degradation towards the film surface. The remote argon plasma was proved to be more effective on forming the oxide group upon the PVC surface.

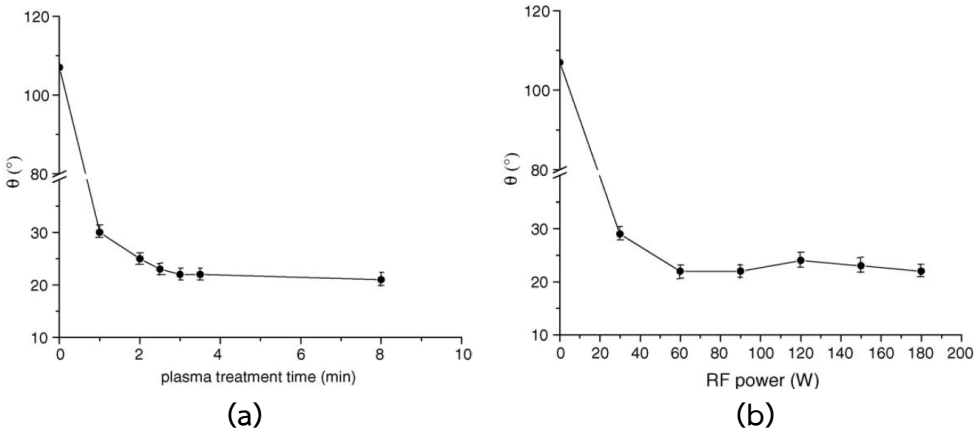

Figure 2.20 Effect of (a) exposure time and (b) RF power on the contact angles to water of PVC [21].

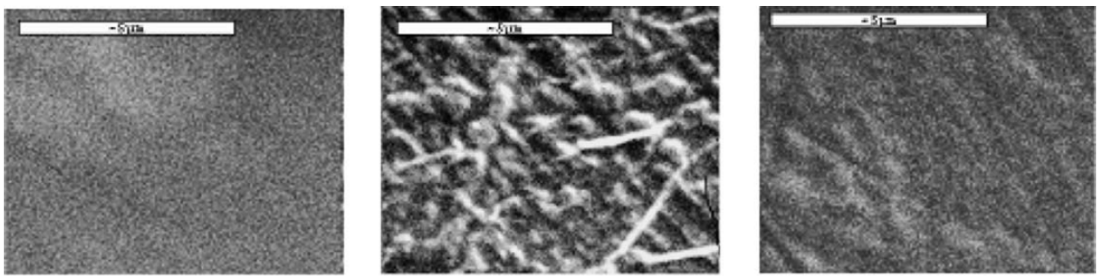

(a) (b) (c)

Figure 2.21 SEM surface images PVC at different condition of (a) original PVC, (b) directed argon plasma treated PVC, and (c) remote argon plasma treated PVC at 60 W for3 minutes [21].

Further, P. Muthimongkol et al. reported the effect of Ar plasma treatment on the Al-doped ZnO. They reported that alteration of the plasma pressure and plasma power can lead to change on surface structures and surface roughness. After argon plasma treatment, the ratio of peak intensity changed, due to the oxygen vacancy left behind after the surface being bombarded by high energy Ar ion. Meanwhile for the morphology of the films, the roughness of Al-doped ZnO tends to decrease by pressure while it mostly increases by power.

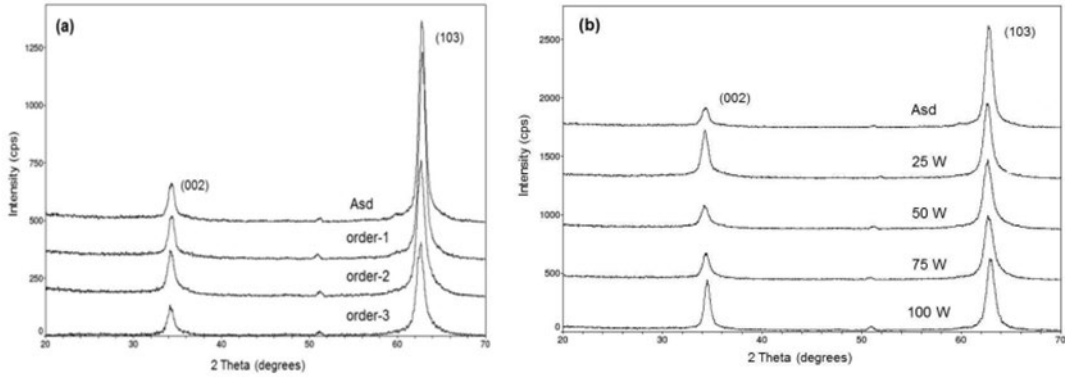

Figure 2.22 XRD patterns of the AZO films were treated at the different (a) operating pressures and (b) plasma power [61].

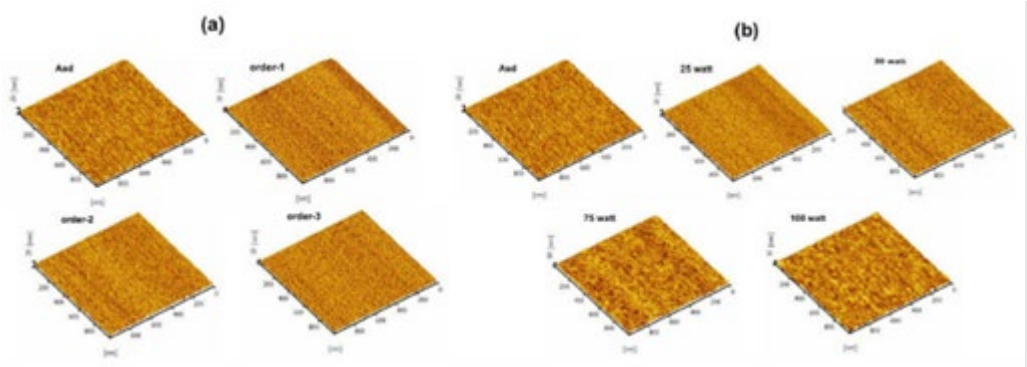

Figure 2.23 AFM images of AZO film were treated by argon plasma at the different (a) operating pressure and (b) plasma power [61].

Table 2.1 The root mean square (rms) value of AZO film was treated by argon plasma at different operating pressure and plasma power.

Sample	rms (nm)
ASD	2.167
Order-1	1.974
Order-2	2.387
Order-3	1.645
25W	2.288
50W	2.387
75W	1.847
100W	2.304

Chapter 3

Research methodology

This chapter describes the details of film production, etching and characterization of film properties. It begins by describing the conditions for the creation of the nanocrystalline $FeSi_2$ and Fe_3Si films by FTDCS. Next, the system and process for etching of the films are described. The last section of this chapter provides the details of several measurement methods for characterization of the physical properties of the films.

3.1 Creation of nanocrystalline $FeSi_2$ and Fe_3Si films

In this research, nanocrystalline $FeSi_2$ and Fe_3Si films were formed onto the surfaces of Si(111) substrates by Asst. Prof. Dr. Nathapron Promros and Japanese students at Kyushu University, Japan. The FTDCS system for the production of nanocrystalline $FeSi_2$ and Fe_3Si films is illustrated in Figure 3.1.

Figure 3.1 FTDCS system for the production of nanocrystalline $FeSi_2$ and Fe_3Si films.

3.1.1 Production of nanocrystalline $FeSi_2$ films on Si(111) wafer substrates

By use of the FTDCS method, nanocrystalline $FeSi_2$ films with 350 nm of thickness were created on Si(111) wafer substrates at room temperature. Prior to the creation of the nanocrystalline $FeSi_2$ thin films, solvents were employed to clean off the oils and organic residues on the surfaces of the Si wafer substrates. Initially, the Si wafer substrates were cleaned with acetone. Then, they were transferred and cleaned by methanol. Next, they were transferred and cleaned with deionized water. Each cleaning step was carried out for a period of 5 minutes. Subsequently, a 1% concentration diluted hydrofluoric solution was applied on the surface of the Si wafer to eliminate the native oxide from the substrate. After being dipped in HF solution, each Si wafer substrate was then transferred and washed in deionized water. After mounted the cleaned Si substrate onto substrate holder, the inside of the FTDCS chamber was ventilated until the pressure reach of 1×10^5 Pa, which was base pressure. The nanocrystalline $FeSi_2$ thin creation was performed in an atmosphere consisting of Ar and H_2 mixed gases flowing at constant flow rate of 15 and 10 sccm, respectively. The operating pressure was maintained at 1.33×10^{-1} Pa during the film creation. Meanwhile, the applied direct current voltage were 950 V and discharge current were 1.2 mA. The conditions for sputtering of the nanocrystalline $FeSi_2$ films can be summarized as shown in Table 3.1.

Table 3.1 Conditions for the creation of nanocrystalline $FeSi_2$ films

Coating conditions for nanocrystalline $FeSi_2$ films	
Substrate	Si (111)
Target of sputtering	$FeSi_2$ (Purity: 6N)
Temperature of substrate	Room temperature
Base pressure	1×10^{-5} Pa
Sputtering pressure	1.33×10^{-1} Pa
Ar gas flow rate	15 sccm
H2 gas flow rate	10 sccm
Discharge voltage	950 V
Discharge current	1.2 mA
Film thickness	350 nm

3.1.2 Production of Fe_3Si films on Si(111) wafer substrates

Fe_3Si films with a film thickness of 1000 nm were produced on p-type Si(111) wafer substrates via FTDCS by utilizing a pair of $FeSi_2$ alloy targets. During the production of the Fe_3Si layer, the substrate temperature was maintained at 300 °C. The Si(111) wafer was cleaned by washing it for 5 minutes in each of acetone, methanol, and deionized water. Following that, a 1% concentration of HF acid solution was used to eliminate the oxide layer. In deionized water, the HF residue was instantly purged from the p-type Si wafer. After cleaning, the Si(111) wafer was mounted to the substrate holder within the FTDCS chamber, leaving 7.5 cm between the wafer and the target. The Fe_3Si films were formed on the Si(111) wafer substrates at a sputtering pressure of 1.33×10^{-1} Pa. The sputtering process was performed in Ar gas with 6N purity. The flow rate of the argon gas was maintained at 15 sccm. The 1 kV voltage was applied for sputtering, while the created sputtering current was approximately 1.2 mA. The conditions for sputtering of the Fe_3Si films can be summarized as shown in Table 3.2.

Table 3.2 Conditions for the creation of Fe_3Si films

Coating conditions for Fe_3Si films	
Substrate	Si (111)
Target of sputtering	Fe_3Si (Purity: 4N)
Temperature of substrate	300 °C
Base pressure	3×10^{-5} Pa
Sputtering pressure	1.33×10^{-1} Pa
Ar gas flow rate	15 sccm
Discharge voltage	1 kV
Discharge current	1.2 mA
Film thickness	1 μm

3.2 Plasma etching apparatus

In the current research, the etching process of nanocrystalline $FeSi_2$ and Fe_3Si films produced via FTDCS method was carried out using Microwave (MW) plasma apparatus installed at Beamline 6a, Synchrotron Light Research Institute (SLRI), Thailand. The plasma etching apparatus is shown in Figure 3.2. This apparatus consists of three main parts: low-pressure plasma system (Diener electronic, model: Pico), microwave generator (Diener electronic, model: MWG 1200), gas feeding system. The film surfaces of the produced nanocrystalline $FeSi_2$ and Fe_3Si films were modified at different power in Ar atmosphere by utilizing this etching apparatus.

Figure 3.2 Plasma etching apparatus for etching the nanocrystalline $FeSi_2$ and Fe_3Si.

As shown in Figure 3.3, the control panel of the plasma system possess multiple command switch and status indicator as listed in table 3.3.

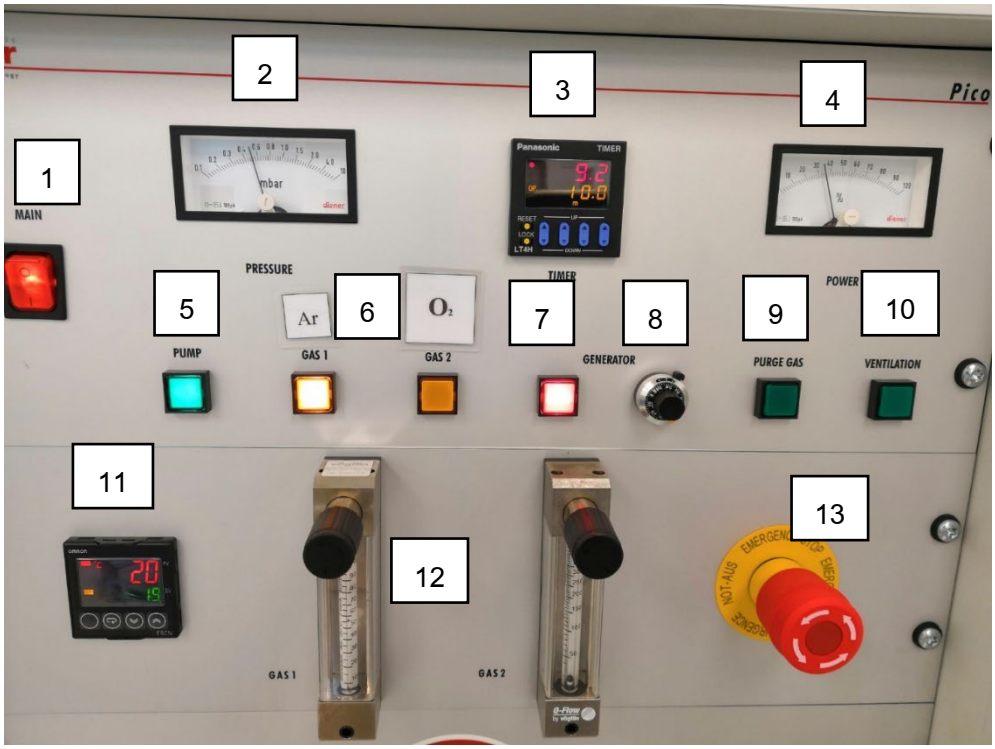

Figure 3.3 The control panel of low-pressure plasma system (Diener electronic, model: Pico).

Table 3.3 List for components of plasma apparatus control panel.

1. Main switch	2. Pressure gauge
3. Timer	4. Power meter
5. Pump switch	6. Gas selector
7. Generation switch	8. Potentiometer Knob
9. Purge switch	10. Ventilation switch
11. Temperature controller	12. Gas flow valve
13. Emergency cancel switch	

3.2.1 Preparation of samples for Etching

Before loading samples into the plasma chamber, the nanocrystalline $FeSi_2$ and Fe_3Si films were divide for each condition and cleaning up with methanol rinsing at the preparation room, as shown in Figure 3.4 (a) and (b)

(a)

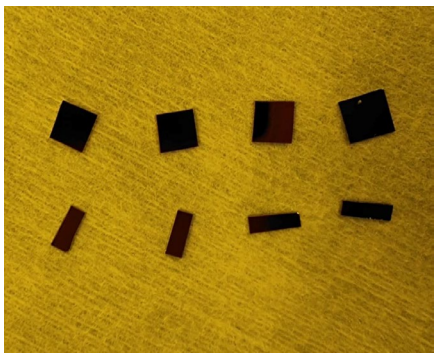

(b)

Figure 3.4 Images of (a) the sample preparation process and (b) the prepared samples.

Next, the prepared samples were moved into cleaned room where the etching apparatus stationed, as shown in Figure 3.5.

Figure 3.5 Images of the cleaned room at Beamline 6a, Synchrotron Light Research Institute, Thailand.

3.3. Etching process

3.3.1 Etching procedure

After the samples were successfully transfered, the researcher switched on the main switch on both pump system and plasma system. Then, turned on the microwave generator, where the maximum output was set to 300 W, as shown in Figure 3.6.

Figure 3.6 The panel of microwave generator (Diener electronic, model: MWG 1200).

Push the ventilation button and wait until the pressure reaching at atmospheric level. After ventilation is completed, open the sample chamber, where etching process will be carried on, and load the sample prepared for etching into the chamber.

Figure 3.7 Vacuum chamber when opened for sample loading.

Shut off the chamber door, hit the pump button, and wait until pressure reaching 0.1 mbar guaging with the pressure guage. After feeding completed, choose the gas to feed onto the system and set the valve to allow the gas to flow at 5 sccm.

Set the timer to 10 minutes and dial the potentiometer knob to certain percentage of generating power, such as 50% for 150 W. Hit generation button to start the plasma etching process.

Figure 3.8 plasma chamber while operating.

After process finished, push ventilation again to feed air into the chamber aand open the chamber to retrieve the etched sample.

3.3.2 Etching condition

Inside the etching chamber, the plasma was built up through the microwave radiation from the magnetron head. The fed Ar gas was ionize by the microwave and generated Ar plasma within vacuum chamber. The etching conditions for all films are depicted in Table 3.4. The etching powers for the nanocrystalline $FeSi_2$ films and Fe_3Si films were set to 50, 100, and 150 W operating for 10 minutes. The as-produced and etched nanocrystalline $FeSi_2$ films and Fe_3Si films are shown in Figure 3.9 and 3.10, respectively.

Table 3.4 etching conditions for the nanocrystalline $FeSi_2$ and Fe_3Si films

Materials	Etching pressure (Pa)	Etching power (°C)	Etching time (hours)
nanocrystalline $FeSi_2$	50	50	10
nanocrystalline $FeSi_2$	50	100	10
nanocrystalline $FeSi_2$	50	150	10
Fe_3Si	50	50	10
Fe_3Si	50	100	10
Fe_3Si	50	150	10

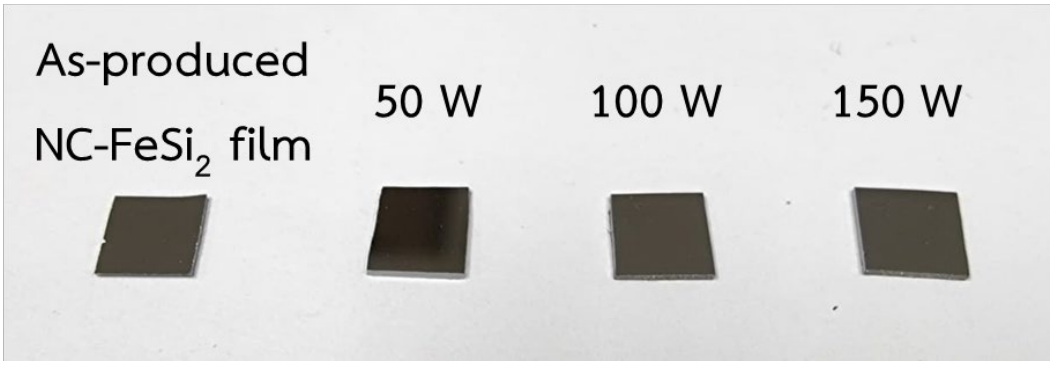

Figure 3.9 The as-produced and etched nanocrystalline $FeSi_2$ films.

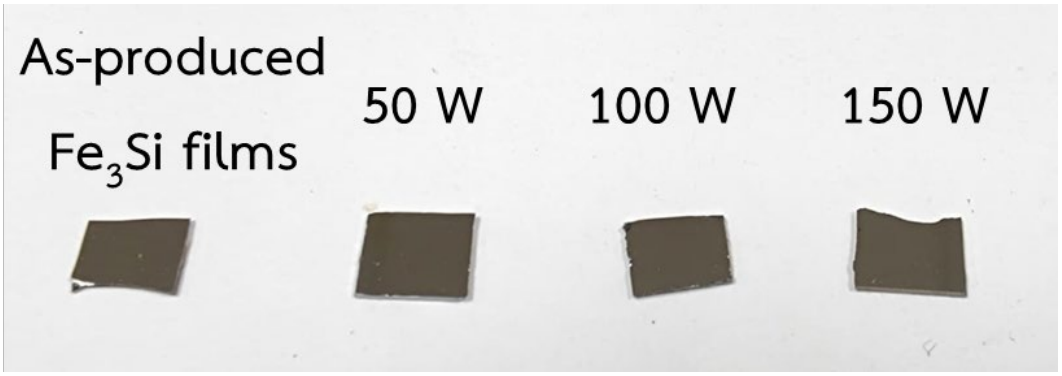

Figure 3.10 The as-produced and etched Fe_3Si films.

3.4 Characterization of the properties of unetched and etched films

Physical properties such as crystallinity, surface morphology, and wettability for the as-deposited and etched films were characterized using the following measurements:

3.4.1 Structure of films

The epitaxial production and crystallinity of the films were examined by utilization of XRD measurement using 2θ for the nanocrystalline $FeSi_2$ and 2θ-θ for Fe_3Si films were measured through this apparatus. The XRD patterns of as-produced and etched nanocrystalline $FeSi_2$ films were characterized by XRD diffractometer (Rigaku, TTRAX III) at National Metal and Materials Technology Center (MTEC) as shown in Fig. 3.11.

Figure. 3.11 The XRD diffractometer (Rigaku, TTRAX III) at MTEC.

3.4.2 Surface composition of films

The atomic concentration of the as-deposited and etched films were monitored by means of XPS (Kratos Analytical, Axis Ultra DLD) at Central equipment unit, ThEP, Chiangmai University, as displayed in Figure 3.12. The atomic concentration and XPS spectra was analyzed through CasaXPS software.

Figure 3.12 XPS equipment (Kratos Analytical, AXIS Ultra DLD).

3.4.3 Surface morphology of the films

The plane surface and cross-section views of the as-created and etched nanocrystalline $FeSi_2$ and Fe_3Si films produced via FTDCS were displayed by utilizing a FESEM (Hitachi, SU 8230) with magnitude in a range from 30k to 300k. Figure 3.13 displays the FESEM apparatus used for examination of the surface morphology of the as-created and etched films.

Figure 3.13 The Hitachi SU 8230 FESEM apparatus.

3.4.4 Surface roughness of the films

The roughness of the surface for as-produced and etched films was investigated by means of AFM. Figure 3.14 illustrates the AFM apparatus (Park system, XE-120) for observing surface roughness under 5 X 5 μm^2. The surfaces of as-produced and etched nanocrystalline $FeSi_2$ and Fe_3Si films were scanned in non-contact mode.

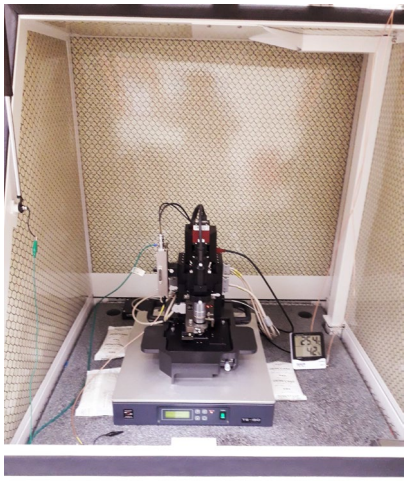

Figure 3.14 AFM apparatus (Park system, XE-120).

3.4.5 Contact angle measurement

To identify the wettability properties of the nanocrystalline $FeSi_2$ and Fe_3Si films before and after the etching process, the contact angle values of dropped water on the surface of films were measured by contact angle OCA 20, as shown in Figure 3.15. In this measurement method, the DI water was dropped from a syringe with a volume of 5 µl and dosing rate of 1 µl/s. Images of the drop on the film surface were captured by a camera on the instrument. The contact angle values were analyzed through SCA 20 Software.

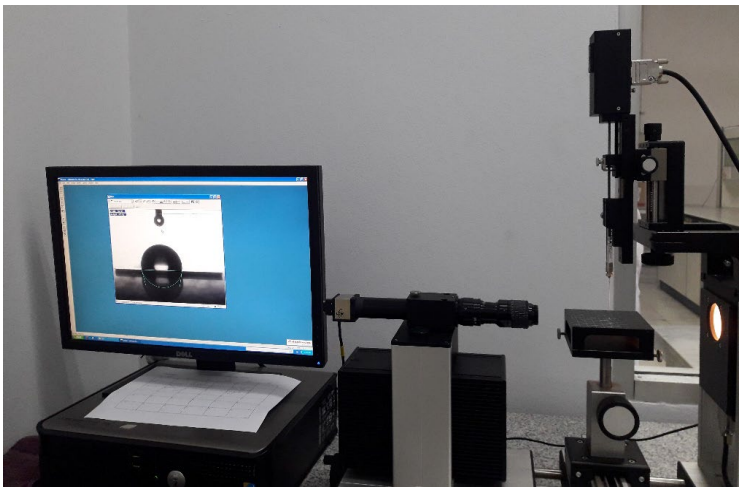

Figure 3.15 Contact angle analyzer (OCA 20) and a display monitor.

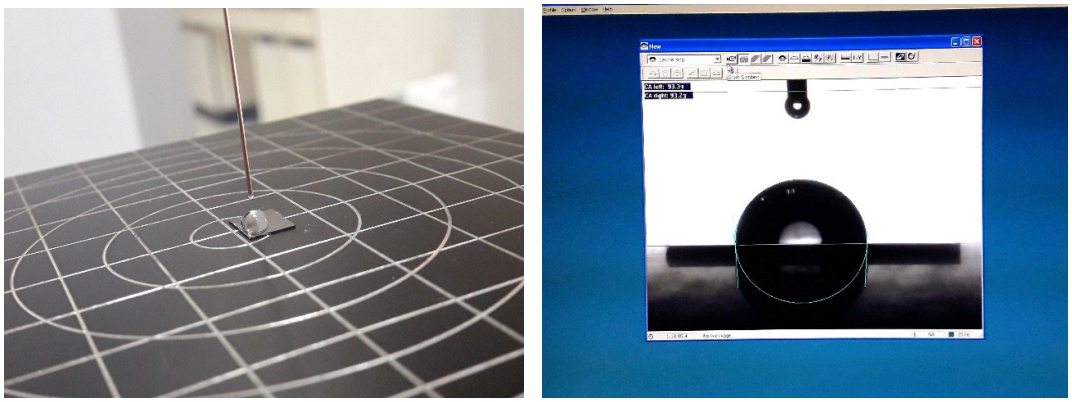

(a) (b)

Figure 3.16 Drop on the surface of films in (a) normal view and (b) view on the monitor with an estimation of contact angle values.

3.4.6 Mechanical investigation

The mechanical property for the surface of as-created and etched nanocrystalline $FeSi_2$ and Fe_3Si films produced via FTDCS was investigated through a nanoindentaion test with a Berkovich indenter's tip. (Bruker Hysistron, model Ti Primier) at National Nanotechnology Center, as depicted in Figure 3.17.

Figure 3.17 Nanoindentation apparatus (Bruker Hysistron, model Ti Primier).

Chapter 4
Results and Discussion

This chapter describes the experimental results of surface morphology, structural, and wetting properties for as-produced and etched samples (nanocrystalline $FeSi_2$ and Fe_3Si thin films). The results of etched films were compared to the as-produced films. The results are presented in a sequence of as-produced nanocrystalline $FeSi_2$, etched nanocrystalline $FeSi_2$, as-produced Fe_3Si, and etched Fe_3Si, respectively.

4.1 Physical properties of as-produced nanocrystalline $FeSi_2$ films

4.1.1 XRD pattern of as-produced nanocrystalline $FeSi_2$ films

Figure 4.1 depicts the obtained XRD patterns for the nanocrystalline $FeSi_2$ films formed by FTDCS. This measurement was carried out with an XRD apparatus utilizing the grazing incidence method (2 θ scan) at a fixed incidence angle of 2°. It was clear that these XRD patterns exhibited a broad peak in the range of 40-50°. The superposition of several diffraction peaks of β-$FeSi_2$ was the likely culprit for this peak The crystallite size could be estimated based on the Scherrer equation using the peak of the XRD pattern, which is as follows [62,63]:

$$D = \frac{0.94\lambda}{\beta \cos\theta} \qquad (3.1)$$

where λ is the X-ray wavelength (λ = 1.542 Å) (CuKα), β is the full width at half maximum (FWHM) in the radian and θ is the diffraction angle. From estimation using the Scherrer equation, the grain sizes of the nanocrystalline $FeSi_2$ films formed by FTDCS was 2.51 nm.

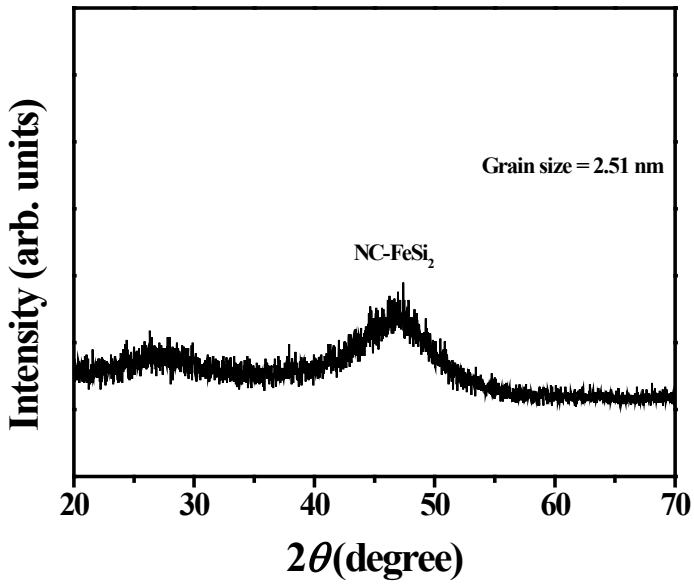

Figure 4.1 XRD patterns at a fixed incidence angle of 2° of the as-produced nanocrystalline $FeSi_2$ films formed by means of FTDCS.

4.1.2 XPS spectrum of as-produced nanocrystalline $FeSi_2$ films

Figure 4.2 displays the XPS line of the nanocrystalline $FeSi_2$ layer coated on a p-type Si(111) wafer via FTDCS compose of the peaks of Fe 2p, O 1s, N 1s, C 1s, and Si 2p. From the obtained spectra, the atomic concentration of the films can be quantified through the relative intensities of the peaks. The chemical composition of the as-produced nanocrystalline $FeSi_2$ film's surface was display in table 4.1. The results of these lines my implied that a dominant source of the $FeSi_2$ film's hydrophobicity may come from the organic carbon [16,20]. There is also the strong presence of oxide layer that can be found easily on the Fe-based material [64,65]. These contaminants cover large chunk of the surface of Fe_3Si films resulting in low amounts of Fe an Si observed. For N 1s, the nitrogen content may have come as a part of organic residues on the exposed surface, which is consistent with the copious amounts of carbon found on the surface [64,65].

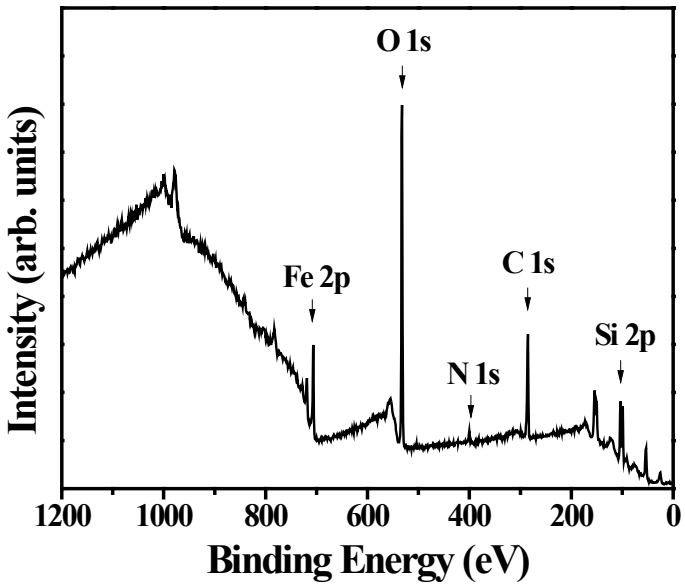

Figure 4.2 XPS lines of as-created nanocrystalline $FeSi_2$ films produced by FTDCS.

Table 4.1 Atomic concentration of nanocrystalline $FeSi_2$ films created by FTDCS.

Sample	Surface Atomic Concentration (at.%)				
	Fe 2p	O 1s	N 1s	C 1s	Si 2p
Unetched nanocrystalline $FeSi_2$ films	2.91	36.93	1.87	34.47	23.83

4.1.3 FESEM image of as-produced nanocrystalline $FeSi_2$ films

Figure 4.3 portrays the FESEM images in plain view of as-produced nanocrystalline $FeSi_2$ thin films created by FTDCS. The unetched nanocrystalline $FeSi_2$ films possessed a very flat surface and consisted of numerous crystallites smaller less than 5 nm aligning in uniform fashion. This can be explained by the fact that, in the creation process of nanocrystalline $FeSi_2$ films employing FTDCS at room temperature, the Si substrate is placed on a substrate holder far away from the plasma that was created by the sputtering process [44-46]. Furthermore, the film surface temperature during film formation was not increased because the Si substrate was located out of the plasma zone [44-46]. This substrate placement allowed the surface of the nanocrystalline $FeSi_2$ films to suffered only very minor damage from plasma. As a result, the nanocrystalline $FeSi_2$ films with relatively flat surface could be formed utilizing FTDCS.

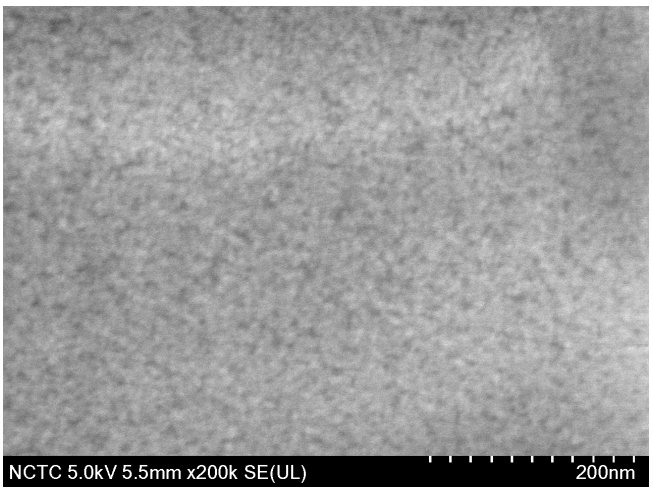

Figure 4.3 FESEM surface of the produced nanocrystalline $FeSi_2$ layer formed via FTDCS.

4.1.4 AFM image of as-produced nanocrystalline $FeSi_2$ films

Figure 4.4 presents a three-dimensional AFM image of the as-produced nanocrystalline $FeSi_2$ film surfaces created by FTDCS at room temperature. Due to the low plasma damage and temperature during sputtering using FTDCS, the surfaces of the as-produced nanocrystalline $FeSi_2$ films were very smooth and continuous [44-46]. The rms roughness (R_{rms})for the surfaces of the as-produced nanocrystalline $FeSi_2$ layer was found to be 1.04 Å.

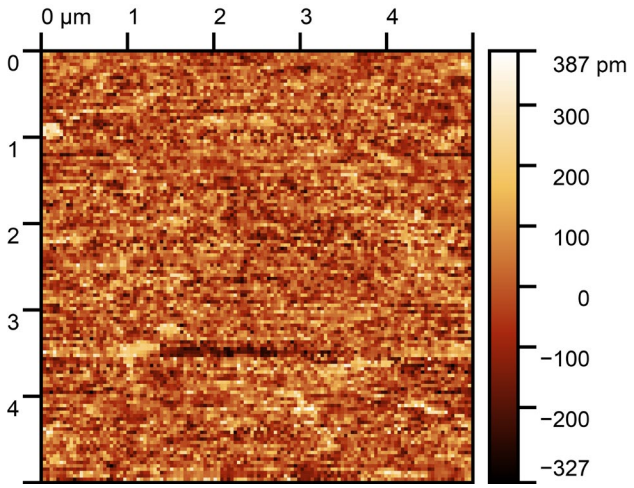

Figure 4.4 Illustration of AFM for the surface of unetched nanocrystalline $FeSi_2$ films.

4.1.5 Wettability of as-produced nanocrystalline $FeSi_2$ films

Figure 4.5 presents an image of the sessile contact angle measurement of as-produced nanocrystalline $FeSi_2$ films formed by FTDCS. The wetting property can be verified based on the average contact angle (θ_{ca}), into super-hydrophobic ($150° \leq \theta_{ca} \leq 180°$), hydrophobic ($90° \leq \theta_{ca} < 150°$), hydrophilic ($10° < \theta_{ca} < 90°$), and super-hydrophilic ($\theta_{ca} \leq 10°$) [47]. In the case of non-etching, the θ_{ca} of water dropped on the nanocrystalline $FeSi_2$ film surface was 100.55°. This experimental result established that the nanocrystalline $FeSi_2$ films had wetting state of hydrophobic surface.

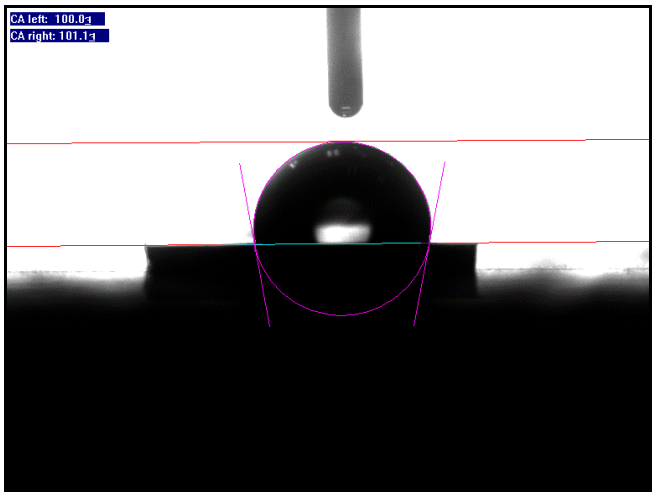

Figure 4.5 Image of water droplet on the surface of the nanocrystalline $FeSi_2$ films.

4.1.6 Mechanical property of as-produced nanocrystalline $FeSi_2$ films

For the mechanical properties, the nanoindentation technique using a Berkovich indenter was used to investigate the hardness and reduced elastic characteristics of the untreated nanocrystalline $FeSi_2$ film surfaces. The indentation test was carried on by applying an indentation load of 3 mN to the nanocrystalline $FeSi_2$ films. The maximum depth for the test was controlled at 10% of the thickness of all films, where the effect of the substrate could be suppressed [66,67]. The nanoindentation test for the was performed repeatedly, five times. Figure 4.6 presents the plot set of the applied indentation load versus the depth of penetration (load–depth curve) for the nanocrystalline $FeSi_2$ films. The average hardness value (H) and reduced elastic modulus value (E_r) of the untreated

nanocrystalline $FeSi_2$ films were calculated from the unloading portions of their load–depth curve [68,69]. The H and E_r for the nanocrystalline $FeSi_2$ samples are summarized in Table 4.2. The result shown that nanocrystalline $FeSi_2$ samples possess significantly lower H and E_r compare to β-$FeSi_2$ from our previous work and conventional coating material like diamond-based films [70-72]

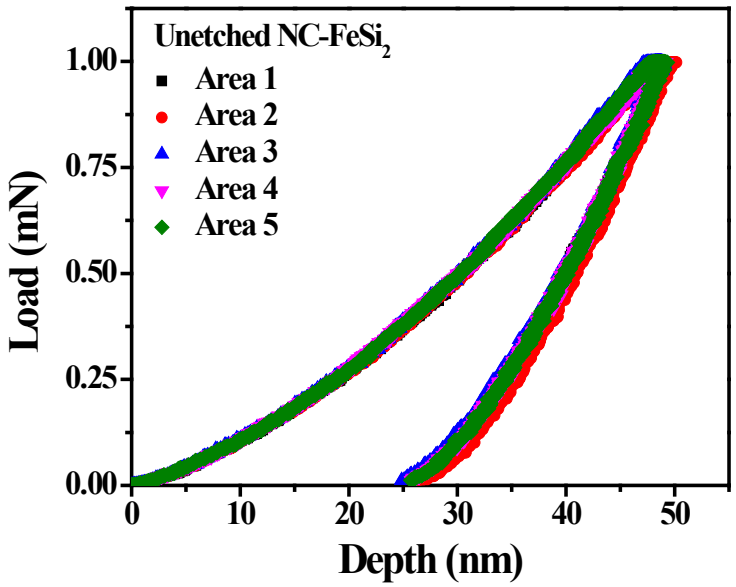

Figure 4.6 Load-depth plots of the nanocrystalline $FeSi_2$ films created by FTDCS.

Table 4.2 H and E_r for unetched nanocrystalline $FeSi_2$ created by FTDCS in comparison with various materials.

Sample	H (GPa)	E_r (GPa)
Unetched nanocrystalline $FeSi_2$	9.616	159.146
β-$FeSi_2$ via FTDCS	37.55	643.42
Fe_3Si via FTDCS	9.392	204.862
DLC film	12-30	68-213
Diamond film	80-100	500-533
Natural diamond	56-102	1050

4.2 Physical properties of unetched and etched nanocrystalline $FeSi_2$ films

4.2.1 XRD patterns of unetched and etched nanocrystalline $FeSi_2$ films

Figure 4.7 depicts XRD patterns for the as-produced nanocrystalline $FeSi_2$ films and Ar etched nanocrystalline $FeSi_2$ films at 50, 100, and 150 W. After etching with 50 W Ar plasma, the board peak was turned into multiple peaks with sharp nanocrystalline $FeSi_2$ (110) peak at 44° and weak nanocrystalline $FeSi_2$ (200) peak at 64°. The peak intensity is observed to increase with etching at 100 W and decrease with etching at 150 W. Due to peak intensity being correlated to crystallinity, higher peak intensity for 100 W etched can be translate to improvement of crystallinity [73]. The improvement may attributed to the volatilization of the surface contaminants and defects as well as the energy transfer from the impact of high energy Ar ion, which lead to preferable crystal orientation [73,74]. Meanwhile, lower peak intensity for 150 W etched can be translate to crystallinity derangement. During Ar plasma etching, high energetic ion bombarded the surface and remove defected portion and contamination out of the films resulting in preferrable orientation [73,74]. In contrary, crystalline structure can be damaged by the ion with sufficient energy resulting in less preferrable orientation [74].

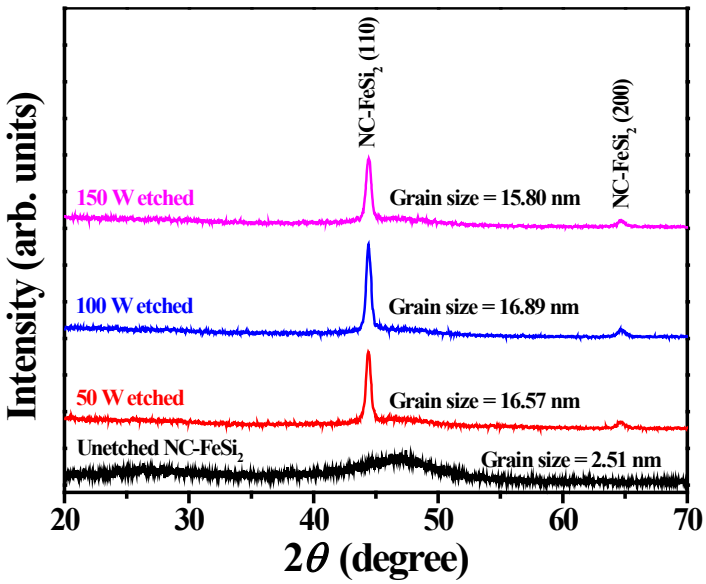

Figure 4.7 XRD spectra for nanocrystalline $FeSi_2$ films without etching and etching at different plasma power.

4.2.2 XPS spectra of the unetched and etched nanocrystalline $FeSi_2$ films

Figure 4.8 demonstrates the XPS results for the surface composition of the etched nanocrystalline $FeSi_2$ films and nanocrystalline $FeSi_2$ films treated at different powers, which were used as a basis for atomic concentration of the film's surface, as represented in Table 4.3. The results showed an opposite behavior between the content of O 1s and C 1s concentrations for all nanocrystalline $FeSi_2$ films. In response to the plasma exposure, the C 1s concentration decreased, while O 1s concentration increased as the MW power was raised. Under the low-pressure MW plasma etching of Ar, high-energy ions collide with the sample surface, dissociate the hydrophobic organic carbon contaminants, and cause them to volatilize [16]. Meanwhile, hydrophilic oxide groups may come from the MW plasma chamber as the Ar gas may contain a tiny amount of oxygen, as well as the highly active groups remaining on the surface after plasma bombardment, which subsequently react with oxygen when exposed to air or plasma impurity [19,20].

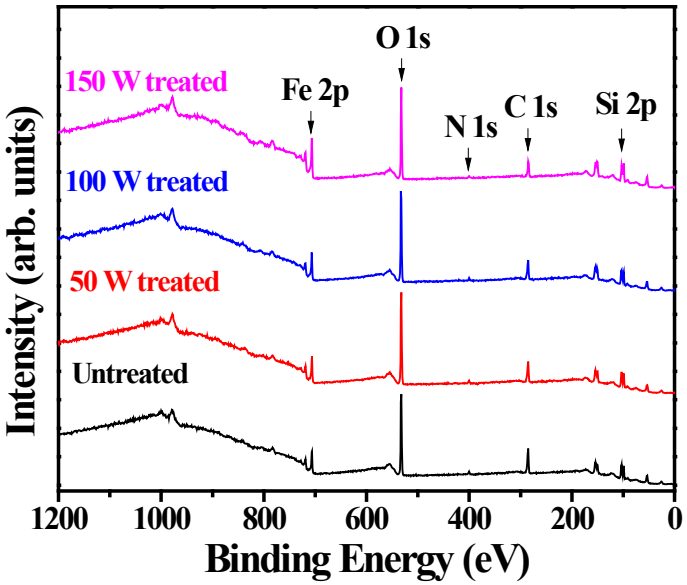

Figure 4.8 XPS spectra of etched nanocrystalline $FeSi_2$ films under various etching power in comparison with as-produced nanocrystalline $FeSi_2$ films.

Table 4.3 Atomic concentration of nanocrystalline $FeSi_2$ films at different MW plasma treatment conditions.

Sample	Surface Atomic Concentration (at.%)				
	Fe 2p	**O 1s**	**N 1s**	**C 1s**	**Si 2p**
Unetched nanocrystalline $FeSi_2$	2.91	36.93	1.87	34.47	23.83
Ar etched (50 W; 10 min)	3.02	38.61	3.13	29.22	26.02
Ar etched (100 W; 10 min)	3.19	40.42	2.57	27.15	26.68
Ar etched (150 W; 10 min)	5.51	35.96	2.57	24.04	31.92

4.2.3 FESEM of unetched and etched nanocrystalline $FeSi_2$ films

Figure 4.9 depicts FESEM images in plain view of nanocrystalline $FeSi_2$ films created by FTDCS in the case of unetched and etched at temperatures of 50, 100, and 150 W. From the obtained FESEM images, it was apparent that the unetched nanocrystalline $FeSi_2$ films had a very smooth surface and consisted of numerous small uniform crystallites. At a plasma power of 50 W, the crystallites in nanocrystalline $FeSi_2$ possessed some holes over its structure due to surface bombardment. The holes one on nanocrystalline surface became wider and appeared more frequent as the power raised. This may have originated through the rise in the etching rate because of the Ar ions kinetic energy elevation [15].

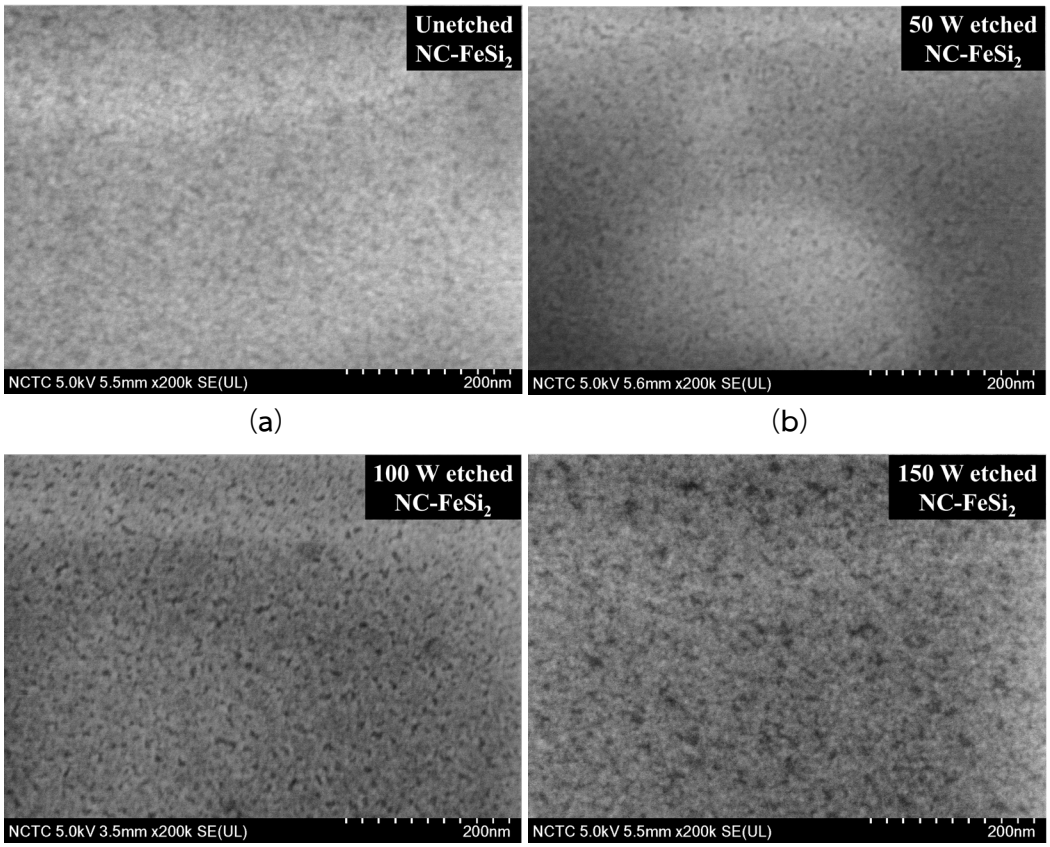

Figure 4.9 Plain-view FESEM micrographs for the as-produced nanocrystalline $FeSi_2$ films at and after etching at 50 W, 100 W, and 150 W.

4.2.4 AFM images of unetched and etched nanocrystalline $FeSi_2$ films

Figure 4.10 shows the surface of the as-produced and etched nanocrystalline $FeSi_2$ films. It can be observed that the surfaces of the unetched nanocrystalline $FeSi_2$ films were very smooth. The R_{rms} of the unetched nanocrystalline $FeSi_2$ film surface was about 1.04 Å. Increasing the etching power caused the rms roughness to gradually increase. The R_{rms} values were 1.21, 2.41, 4.25 Å at etching power of 50, 100, and 150 W, respectively. The pinholes that appeared on the film surface should be the cause of the roughening.

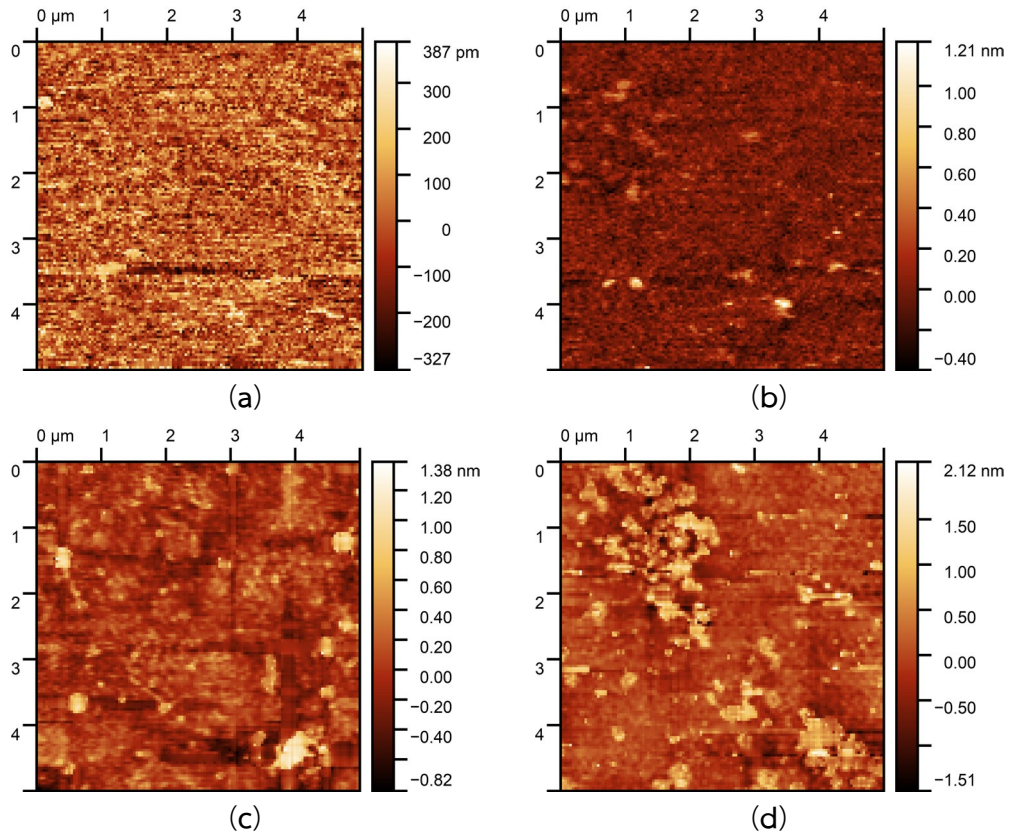

Figure 4.10 AFM images of the nanocrystalline $FeSi_2$ films in the case of unetched and etched under various power of 50, 100, and 150 W.

4.2.5 Wettability of unetched and etched nanocrystalline $FeSi_2$ film surface

Figure 4.11 represents the wetting angle between the droplet and the surface of the unetched Fe_3Si films, where the evaluated θ_{ca} was determined to be 100.55°. After treating with Ar plasma, θ_{ca} was reduced to 53.90° for the nanocrystalline $FeSi_2$ films after treated at 50 W, in which the surface was determined as a hydrophilic state. At increasing powers, the θ_{ca} values for the Fe_3Si films gradually decreased to 43.60° and 35.65° at 100 W and 150 W, respectively.

It was observed that the surface of the unetched nanocrystalline $FeSi_2$ films exhibited their hydrophobicity, while the surfaces of all plasma-etched nanocrystalline $FeSi_2$ films turned into the hydrophilic state. This behavior can be normally explained by the Wenzel model as well as Cassie and Baxter model [53,54]. Based on the FESEM and AFM results, the surfaces of all the nanocrystalline $FeSi_2$ films comprised nano-rough morphology. However, our result shows a significant

alteration of the wetting behavior of nanocrystalline $FeSi_2$ despite the insignificant change in surface morphology. Hence, the wettability of the Fe_3Si films was predominantly dictated by their chemical composition on the surface of the unetched and plasma-etched films. The gained results of XPS revealed that more than a third of the unetched nanocrystalline $FeSi_2$ film's surface was covered by the carbon functional group following by the oxide group and nanocrystalline $FeSi_2$ compositional elements. Hence, the hydrophobicity for the surface should be predominantly controlled due to this reason [16]. After the plasma etching, the XPS results for the etched films revealed a decrease of the hydrophobic carbon chemical composition by selective etching through energetic Ar ions impact [16]. The oxygen concentration also increased due to the highly polarized group left behind after sputter etching at low-pressure MW plasma under an Ar atmosphere [19]. These changes in surface composition resulted in the change in the wetting state from hydrophobic to hydrophilic. The trend continued as the power was increased.

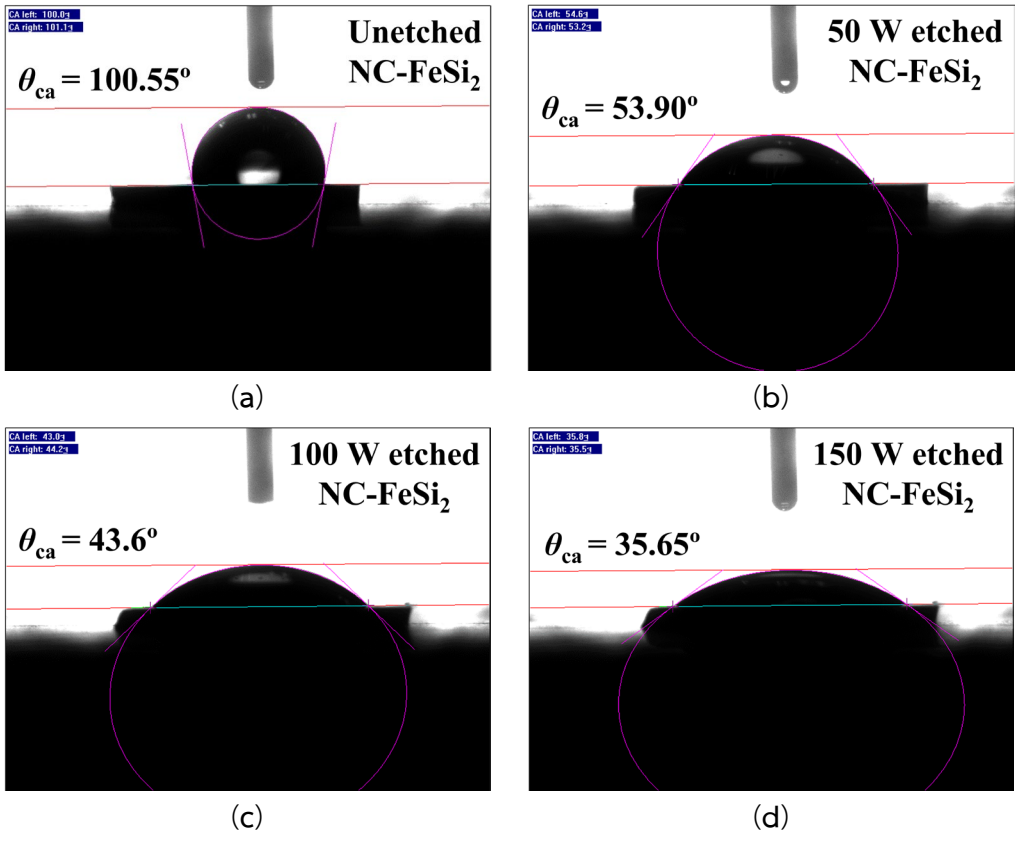

Figure 4.11 Images of contact angles for the as-produced nanocrystalline $FeSi_2$ films and nanocrystalline $FeSi_2$ films etched at 50, 100, and 150 W.

4.2.6 Mechanical property of unetched and etched nanocrystalline $FeSi_2$ film surface

Figure 4.12 presents plots of load versus depth from nanoindentation test on the film's surface of nanocrystalline $FeSi_2$ films in cases of unetched and etched. For the unetched nanocrystalline films, the surface revealed the H of around 9.616 GPa, where the E_r was around 159.146 GPa. For the etched nanocrystalline $FeSi_2$ at varied power, the etched films at power of 50 W exhibited a H of 9.493 GPa and 164.967 GPa for the E_r. With an increasing of power, the H and E_r for the 100 W etched nanocrystalline $FeSi_2$ films were 9.488 GPa and 168.424 GPa, where they altered to 9.425 GPa and 169.146 GPa after etching at 150 W. The H and E_r were almost the same with slightly declined after the Ar plasma treatment, corelating with the morphology results of the films, where the inconsistency of the film's surface was observed as the standard deviation [75]. As the plasma power increased, the deviation increasingly swayed by the accumulated plasma damage [75].

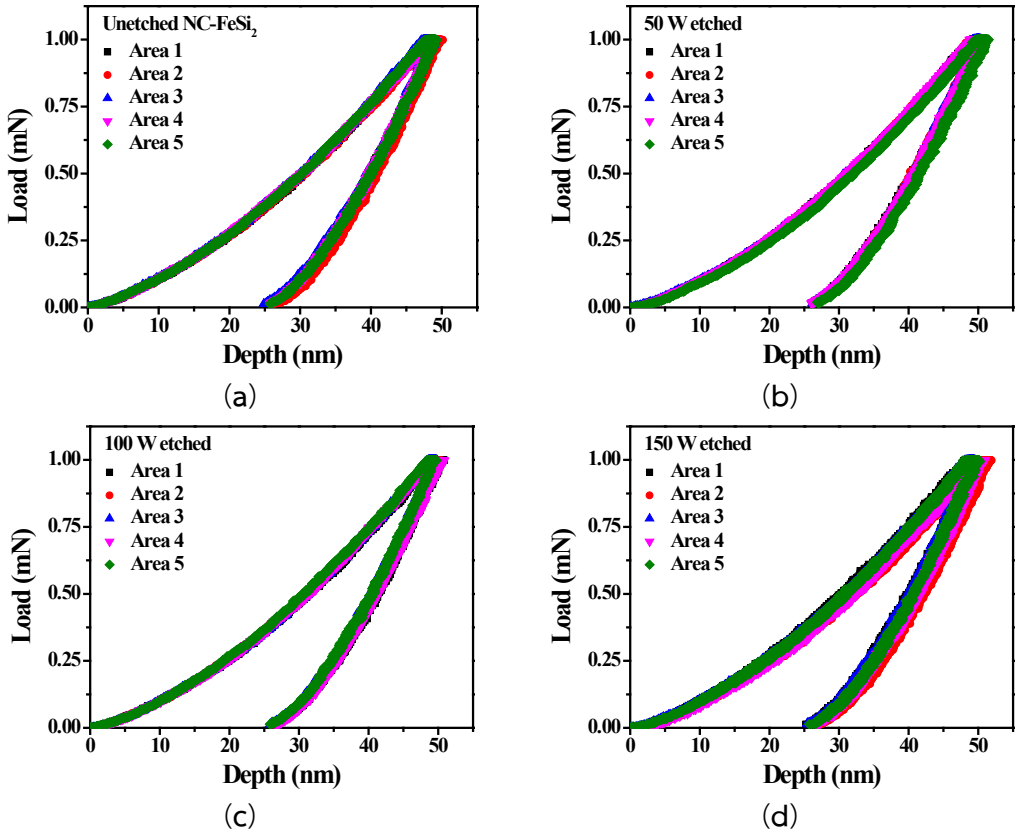

Figure 4.12 Load-depth plots of the nanocrystalline $FeSi_2$ films etched at 50, 100, and 150 W.

Table 4.4 H and E_r for unetched nanocrystalline $FeSi_2$ and Ar plasma etched nanocrystalline $FeSi_2$.

Sample	H (GPa)	E_r (GPa)
Unetched nanocrystalline $FeSi_2$	9.616 ± 0.060	159.146 ± 2.502
Ar etched (50 W; 10 min)	9.493 ± 0.088	164.967 ± 3.798
Ar etched (100 W; 10 min)	9.488 ± 0.100	168.424 ± 4.503
Ar etched (150 W; 10 min)	9.425 ± 0.155	169.146 ± 4.425

4.3 Physical properties of as-produced Fe_3Si films

4.3.1 XRD pattern of as-produced Fe_3Si films

Figure 4.13 presents the XRD patterns for the Fe_3Si films, created at 300 °C substrate temperature. The unetched Fe_3Si films showed the sharp peaks of $Fe_3Si(220)$ and $Fe_3Si(222)$, including the weak peaks of $Fe_3Si(400)$ and $Fe_3Si(422)$ at the positions of 44.42°, 56.26°, 64.70°, and 81.88°, respectively. These obtained peaks are well-known as successful coatings for Fe_3Si films onto Si substrate. The preferential orientations of $Fe_3Si(220)$, $Fe_3Si(222)$, $Fe_3Si(400)$, and $Fe_3Si(422)$ were also reported and confirmed by the literature of S.I. Hirakawa et al. [73] and C.B. Tang et al. [74]. For the details, the orientation of $Fe_3Si(222)$ denoted that the films hold a B_2 structure [4]. The preferred orientations of $Fe_3Si(220)$, $Fe_3Si(400)$, and $Fe_3Si(422)$ showed a fundamental reflection of Fe_3Si films [4].

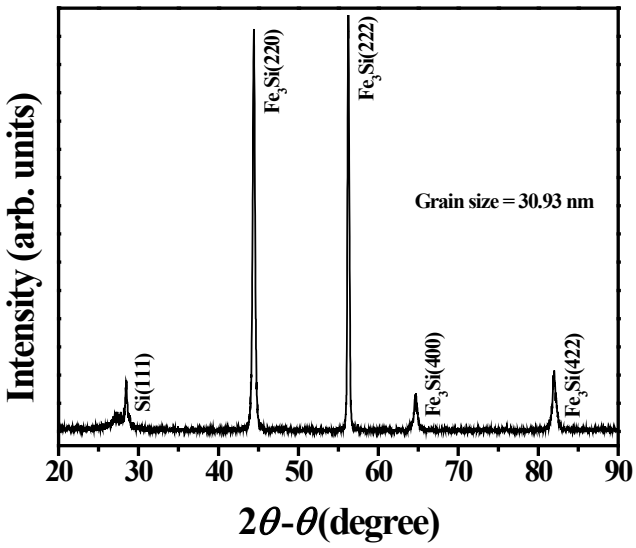

Figure 4.13 XRD patterns of the as-produced Fe_3Si films formed by means of FTDCS.

4.3.2 XPS spectrum of as-produced Fe_3Si films

Figure 4.14 demonstrates the XPS results for the surface composition of the unetched Fe_3Si films formed by means of FTDCS at 300 °C substrate temperature. From the XPS results, the peaks of Fe 2p, O 1s, N 1s, C 1s, and Si 2p were observed. These peaks were translated into an atomic concentration of the film's surface, as represented in Table 4.5. The XPS analysis revealed that, aside from Fe and Si, the surface of the Fe_3Si films also features abundant carbon and oxygen. Carbon and oxygen are common contaminants found in any material, especially on the metal-contained ones after exposing to the environmental air [64,65]. Fe_3Si is an oxidation-prone material that allows the layer of the oxide group to form on its surface easily [64]. The C 1s peak mainly originated from the layer of adventitious carbon, which forms easily on atmospherically exposed metal [65]. These adventitious carbons are commonly attributed to be the reason behind hydrophobicity [16].

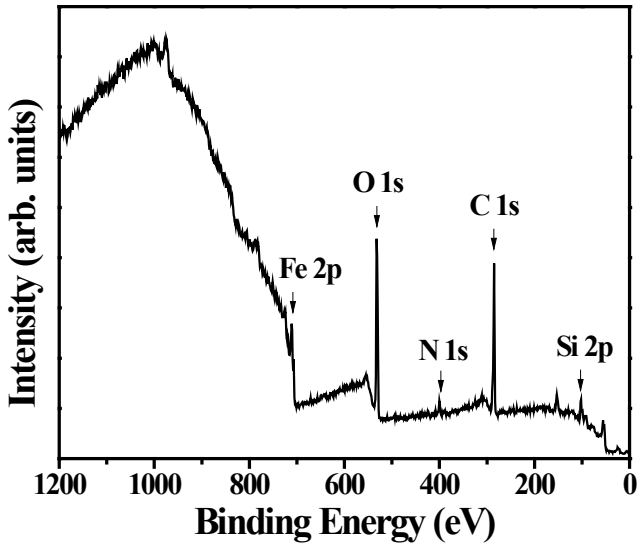

Figure 4.14 XPS spectra of unetched Fe_3Si films formed by means of FTDCS.

Table 4.5 Atomic concentration of Fe_3Si films at different MW plasma treatment conditions.

Sample	Surface Atomic Concentration (at.%)				
	Fe 2p	O 1s	N 1s	C 1s	Si 2p
Unetched Fe_3Si	10.30	47.19	3.28	35.68	3.55

4.3.3 FESEM image of as-produced Fe_3Si films

Figure 4.15 shows typical FESEM micrographs from a top view of the unetched Fe_3Si film surfaces created at 300 ℃ substrate temperature. These micrographs were captured at the magnification of 300 kx. Figure 4.15 exposes that the unetched Fe_3Si films presented an abundance of small crystallites over the entire surface area with a uniform surface structure; pinholes with a destructive surface area were not observed. This should be because of the advantages of FTDCS. Specifically, the fact that FTDCS has the benefits from a small increase in substrate temperature, high plasma density, and low-different stoichiometry between the sputtering target and films layer [44–46]. For the FTDCS, the surface of the Si wafer substrate was in parallel and positioned away from the generated plasma zone during a sputtering of the film, which led to the plasma's particles being confined within the generated magnetic field originated from the permanent magnet beneath the sputtering targets [44–46]. As a result, this sputtering schematic dealt less plasma damage over the film surface [44–46]. The cross-section view of unetched Fe_3Si films shown seamless interface between films layer and Si with the film's thickness of 1.11 μm.

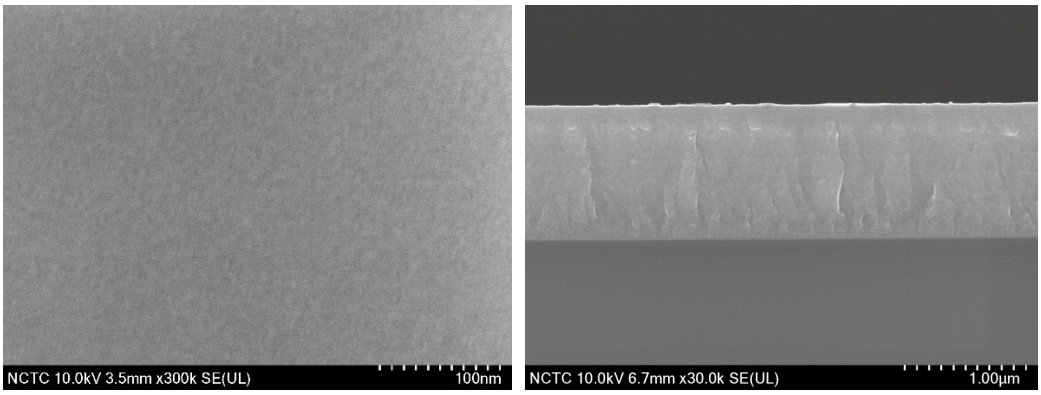

(a) (b)

Figure 4.15 FESEM (a) surface and (b) cross-section of the produced Fe_3Si layer formed via FTDCS.

4.3.4 AFM image of as-produced Fe_3Si films

Figure 4.16 represents the AFM scanned images of the unetched Fe_3Si films. According to the AFM topography, it was visible that the untreated Fe_3Si films exhibited a rather smooth surface with an appraised R_{rms} of 10.63 Å. This outcome was consistent with that of the FESEM result, where the smoothness of the untreated Fe_3Si films should be due to the advantages of facing targets sputtering. As a result, the damage from the plasma should have been low and generated less surface roughness over the film's surface plane [44–46].

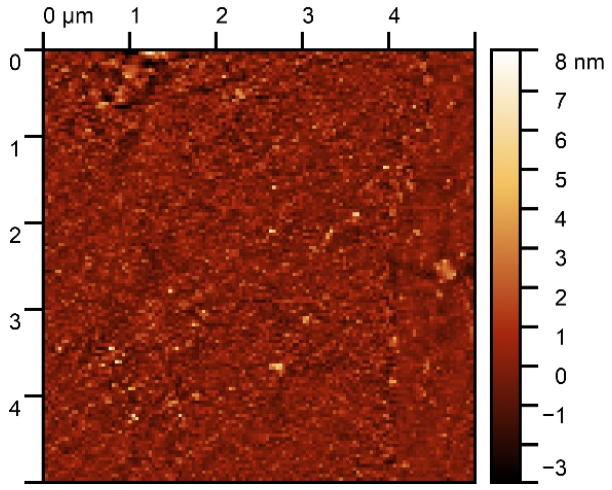

Figure 4.16 Illustration of AFM for the surface of unetched Fe_3Si films.

4.3.5 Wettability of as-produced Fe_3Si films

Figure 4.17 displays the captured images for the contact angle measurement of the unetched Fe_3Si films. For the surfaces of the untreated and treated Fe_3Si films, the wetting angles were determined by using D.I. water droplets. The obtained contact angle is in the range of $90° < \theta_{CA} < 150°$. The wetting angle between the droplet and the surface of the untreated Fe_3Si films, where the evaluated θ_{CA} was determined to be 101.7°. The result shows that the Fe_3Si films exhibited a wetting state of hydrophobic.

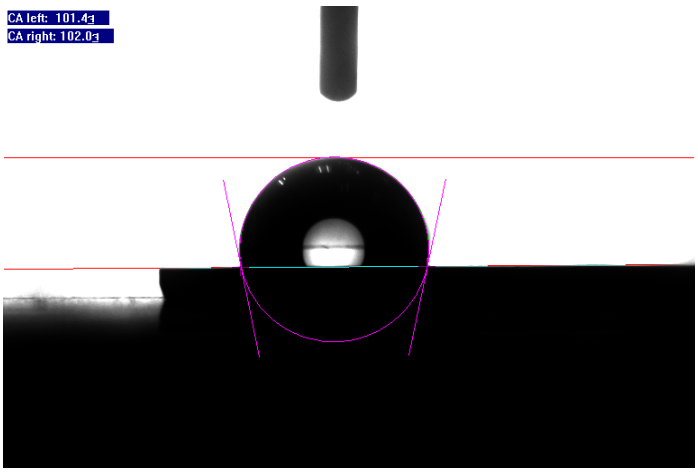

Figure 4.17 Image of water droplet on the surface of the Fe_3Si films.

4.3.6 Mechanical property of as-produced Fe_3Si films

The Berkovich indenter was used to investigate the mechanical properties, such as hardness and reduced elastic characteristics, of the untreated Fe_3Si film surfaces. The indentation test was performed under similar condition as the nanocrystalline $FeSi_2$. Figure 4.18 presents the load–depth curve of the unetched Fe_3Si films, which can be used to calculate the average H and E_r of the untreated Fe_3Si films. The calculated H and E_r values for unetched Fe_3Si films using the unloading portions of their load–depth curve is summarized in Table 4.6. The H and E_r of the untreated Fe_3Si films were relatively similar to nanocrystalline $FeSi_2$ films presented in this work and Fe_3Si films reported by other research groups [77,78].

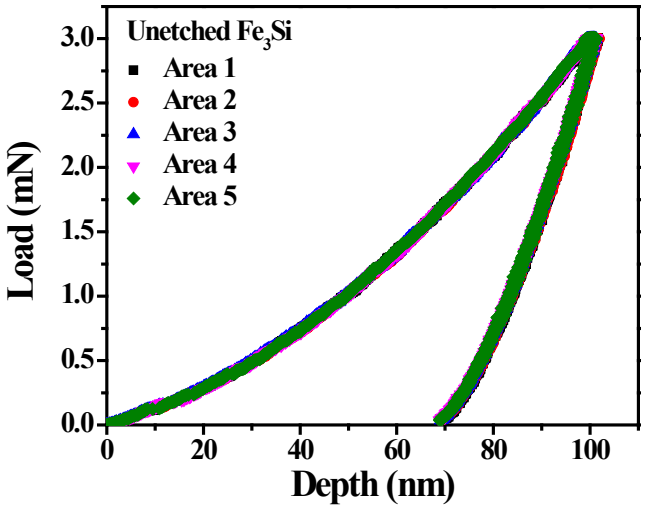

Figure 4.18 Load-depth plots of the Fe_3Si films created by FTDCS at 300°C.

Table 4.6 H and E_r for unetched Fe_3Si created by FTDCS at 300°C in comparison with various materials.

Sample	H (GPa)	E_r (GPa)
Unetched Fe_3Si	9.392	204.862
Nanocrystalline FeSi2 via FTDCS	9.616	159.146
β-$FeSi_2$ via FTDCS	37.55	643.42
Fe3Si via molten-salt infiltration	10.944	275.448
Fe3Si via molten-salt infiltration	8.8	-
DLC film	12-30	68-213
Diamond film	80-100	500-533
Natural diamond	56-102	1050

4.4 Physical properties of unetched and etched Fe_3Si films

4.4.1 XRD patterns of unetched and etched Fe_3Si films

Figure 4.19 presents the XRD patterns for the Fe_3Si films before and after Ar plasma treatment at different powers. The plasma-treated Fe_3Si films were also observed for the peaks of $Fe_3Si(220)$, $Fe_3Si(222)$, $Fe_3Si(400)$, and $Fe_3Si(422)$ like the unetched films. From the XRD peak profiling, the untreated Fe_3Si exhibited the full width at half maximum (FWHM) of the sharpest diffraction peak with a value of 0.379. After treating with 50, 100, and 150 W, the change in the FWHM was observed with the values of 0.322, 0.342, and 0.361, respectively. Based on the appraisement by Scherrer's equation through the JADE software, the crystallite size for the untreated films was around 30.925 nm. The crystallite size became 35.200, 33.175, and 31.225 nm after treating with Ar plasma at 50, 100, and 150 W, respectively. This behavior shows a rise in the crystallite size of the Fe_3Si films after the 50 W plasma treatment, which may originate from the enhancement in crystallinity of the Fe_3Si films [73]. The crystallinity improvement may be due to the defect annihilation progression [73,74]. The crystallite sizes for the Fe_3Si films treated at 100 and 150 W were both relatively smaller than that of the 50 W treated films due to orientational disarrangement caused by the more energetic ions that bombarded the surface [74].

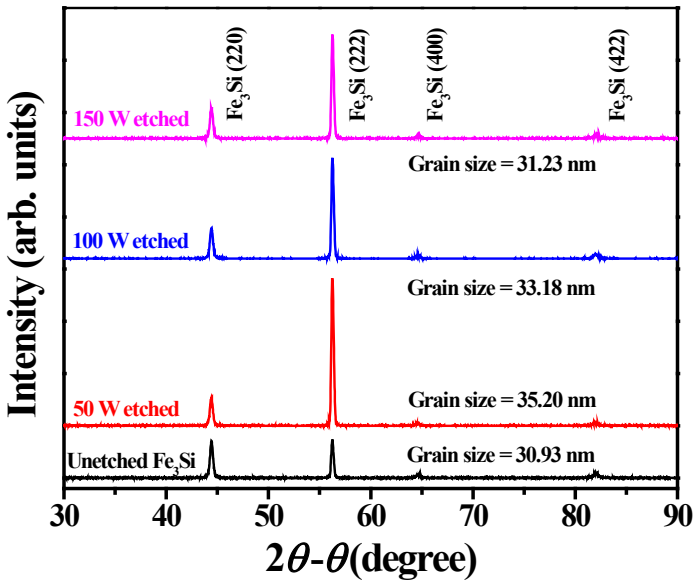

Figure 4.19 XRD patterns of the as-produced and etched Fe_3Si films.

4.4.2 XPS spectra of the unetched and etched Fe_3Si films

Figure 4.20 displays the XRD lines for the as-created and etched Fe_3Si layers created via FTDCS method. Based on the table 4.7, the result extracted from the peak show that the created film surfaces were full of contamination such as oxide group and carbon group. After etching by Ar plasma, the content of oxide group possessed upward trending because of either the oxide formation during the etching session or aging effect [19,20]. Meanwhile, carbon content went down through ejection of carbon atom after its clash against the high energy Ar ion. the trend continued as the ion energy raised through increasingly plasma power [16]. The contents of Fe and Si increased also increased after etching due to reduction of contaminants.

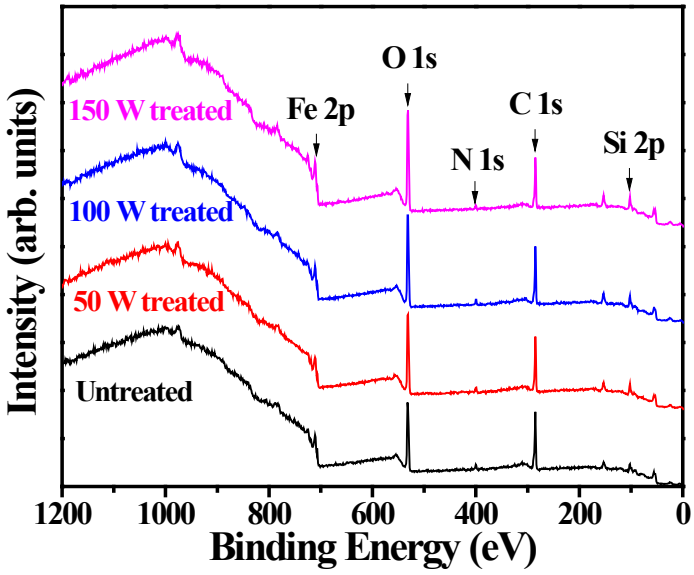

Figure 4.20 XPS spectra of etched Fe_3Si films under various etching powers in comparison with as-produced Fe_3Si films.

Table 4.7 Atomic concentration of Fe_3Si films at different MW plasma etching conditions.

Sample	Surface Atomic Concentration (at.%)				
	Fe 2p	O 1s	N 1s	C 1s	Si 2p
Unetched Fe_3Si	10.30	47.19	3.28	35.68	3.55
Ar etched (50 W; 10 min)	12.78	53.07	2.87	26.47	4.81
Ar etched (100 W; 10 min)	13.61	56.15	2.00	23.48	4.76
Ar etched (150 W; 10 min)	15.49	56.23	2.02	20.35	5.92

4.4.3 FESEM images of the unetched and etched Fe_3Si films

Figure 4.21 shows FESEM micrographs from a top view of the unetched and etched Fe_3Si film surfaces by Ar plasma etching under the various etching powers. The surface structure of the 50 W etched Fe_3Si films was slightly changed from that of the unetched Fe_3Si films. At the higher powers of 100 and 150 W, the influence of the plasma etching on the morphology of the etched Fe_3Si film's surface became more noticeable with the formation of slight bumps, including a non-smooth surface pattern and pinholes. The change of the etched Fe_3Si film's surface increased as the power was increased.

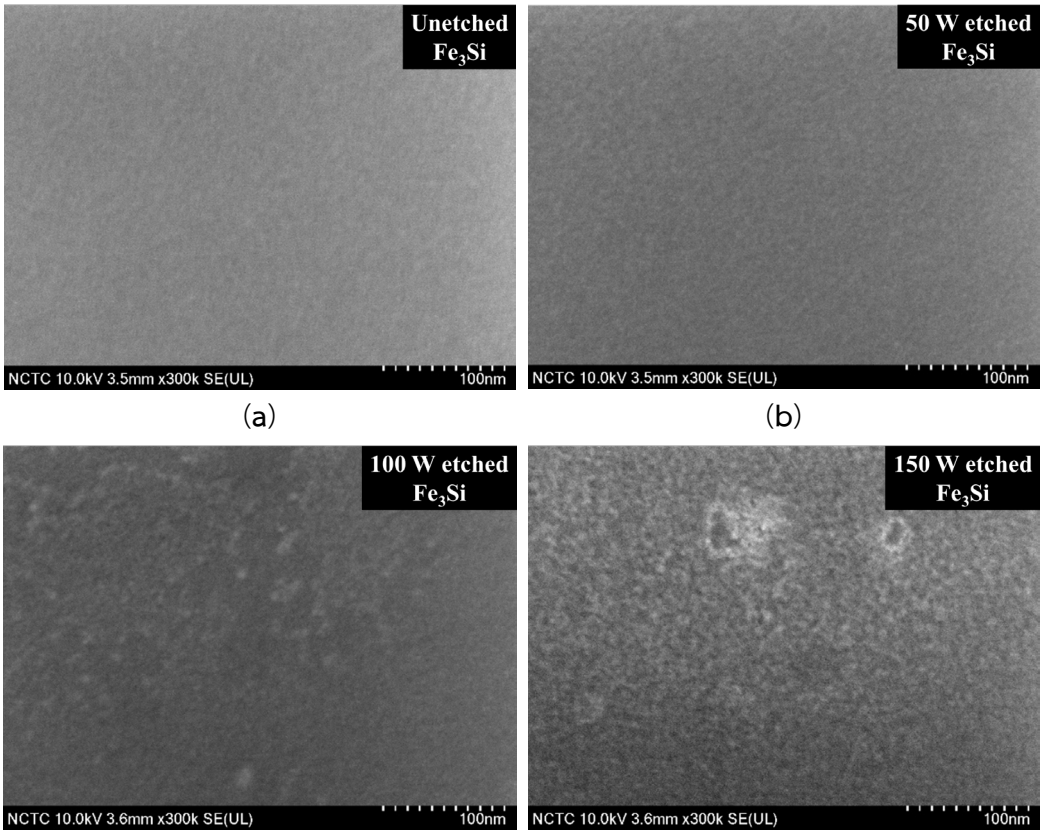

Figure 4.21 FESEM images in plane surface view of as-created Fe_3Si films and after etching at powers of 50 W, 100 W, and 150 W.

The cross-section view shown in Figure 4.22 is for as-produced Fe_3Si films and after etching at 50, 100, and 150 W of plasma power. From observation of film interface, all the Fe_3Si films also showed a clean interface between the films and the substrate. The etched Fe_3Si exhibited reduction of the films thickness as the power in creased due to increased of etch rate. The Fe_3Si films possess post-etched thickness of 1.09, 1.08, and 1.05 μm for 50, 100, and 150 W etching, respectively.

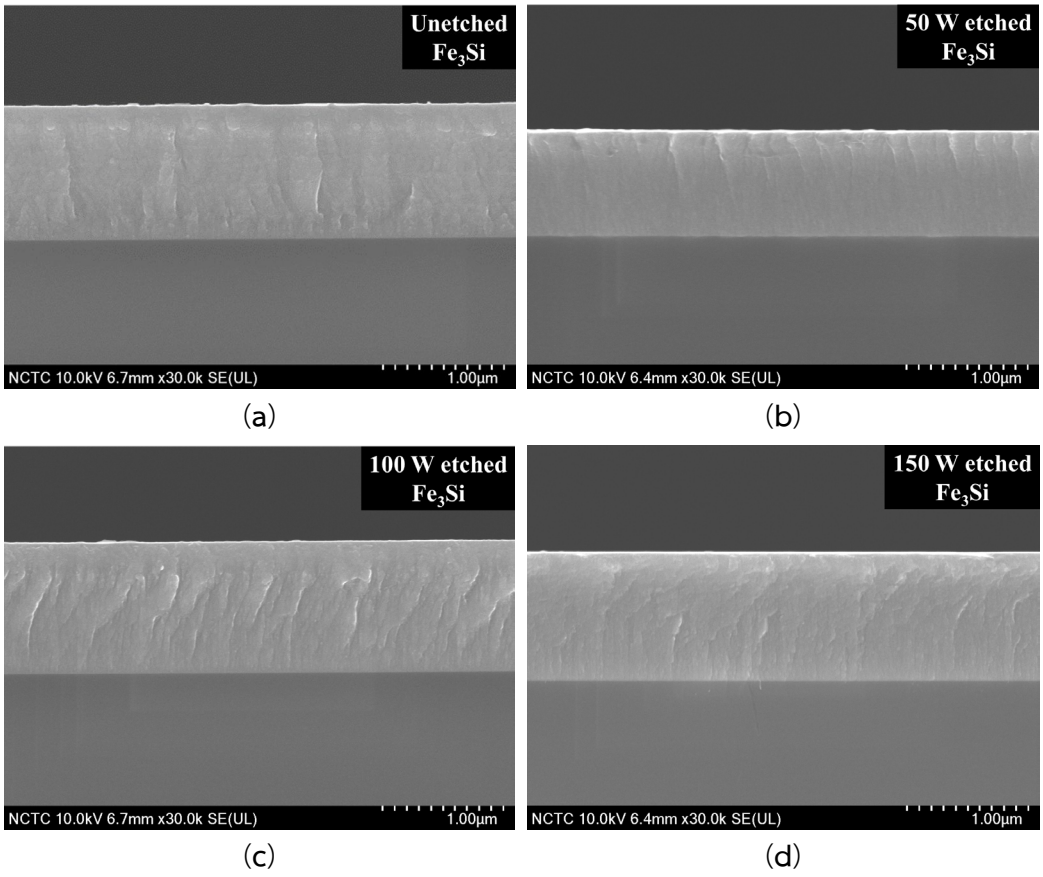

Figure 4.22 Crossectional view of as-created Fe_3Si films and after etching at powers of 50 W, 100 W, and 150 W.

4.4.4 AFM images of unetched and etched Fe_3Si films

Figure 4.23 represents the AFM scanned images of the unetched and etched Fe_3Si films through Ar plasma at the different applied powers. The unetched Fe_3Si films exhibited a rather smooth surface with an appraised R_{rms} of 10.63 Å. After the etching with Ar plasma, the R_{rms} value for the Fe_3Si films etched with 50 W power was evaluated to be 10.71 Å, where the R_{rms} value was slightly higher than that of the Fe_3Si films without plasma etching. The etched Fe_3Si films at 100 and 150 W manifested the assessed R_{rms} values of 11.07 and 13.06 Å, respectively. In the process of MW plasma etching, the Fe_3Si film surface was bombarded by highly energetic species ejecting some Fe and Si atoms from the Fe_3Si surface out, resulting in a physical change in the surface roughness [15].

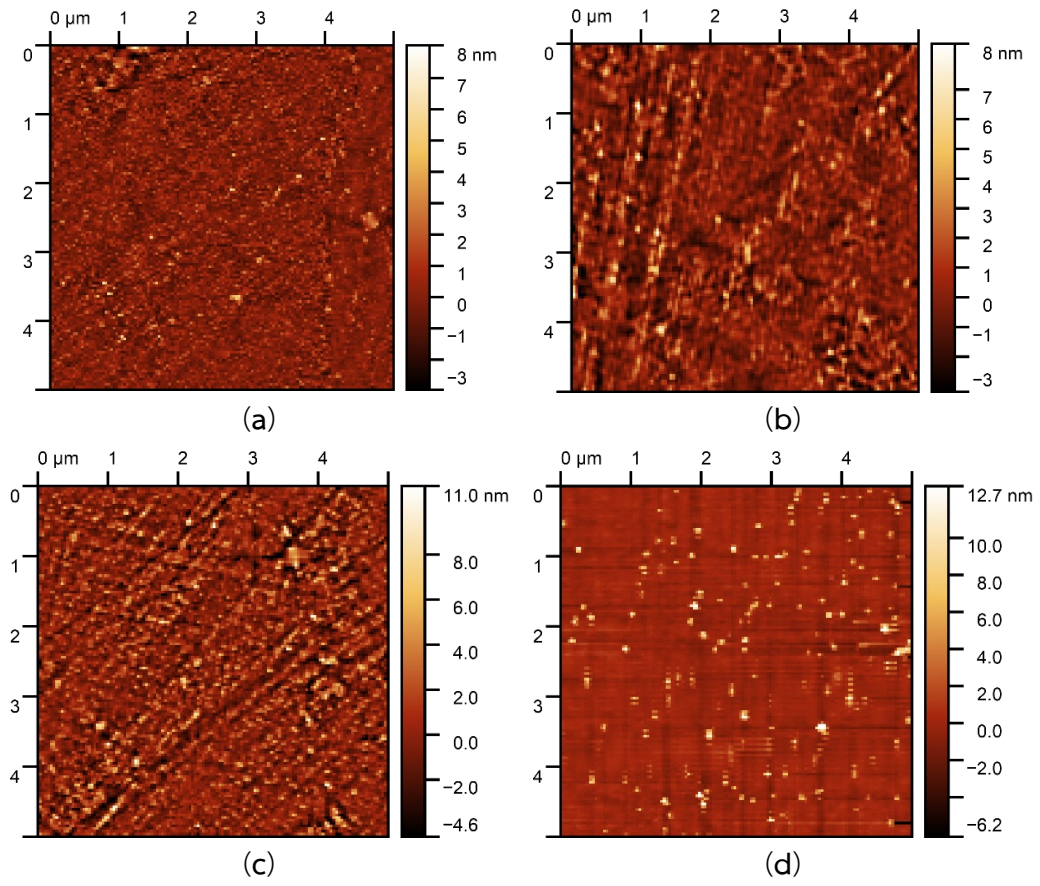

Figure 4.23 AFM images of the Fe_3Si film surfaces in case of unetched and etched at power of 50, 100, and 150 W.

4.4.5 Wettability of unetched and etched Fe_3Si films

Figure 4.24 presents images of the measured contact angles for as-created and etched Fe_3Si films at 50, 100, and 150 W. For water dropped on the as-produced Fe_3Si film surface, the θ_{ca} was 101.70°. When the Fe_3Si thin films were etched at a power of 50 W, the θ_{ca} was slightly decreased to 87.75° and turned to hydrophilic surface. According to the acquired surface morphology from the FESEM and AFM image of the Fe_3Si films under power at 50 W, the R_{rms} were increased in comparison with those of unetched Fe_3Si films due to pinhole. In physical terms, the surface wetting of the Fe_3Si films can be commonly attributed to the wetting models of Wenzel and Cassie-Baxter [53,54]. Wenzel and Cassie-Baxter incorporated the roughness as one of the important parameters in their models, where the former is based on surface alignment and the latter relies on the air groove [53,54]. However, due to insignificant change on the physical properties on the Fe_3Si films after etching,

the change of wetting state should come from chemical composition of the film's surface. After the etching power were increased to 100 W and 150 W, the θ_{ca} values were decreased to 79.20° and 67.05°, respectively. The change in wetting properties corresponds to XPS results. The hydrophobic carbon reduction and hydrophilic oxide increment result correlated with the trend of contact angle.

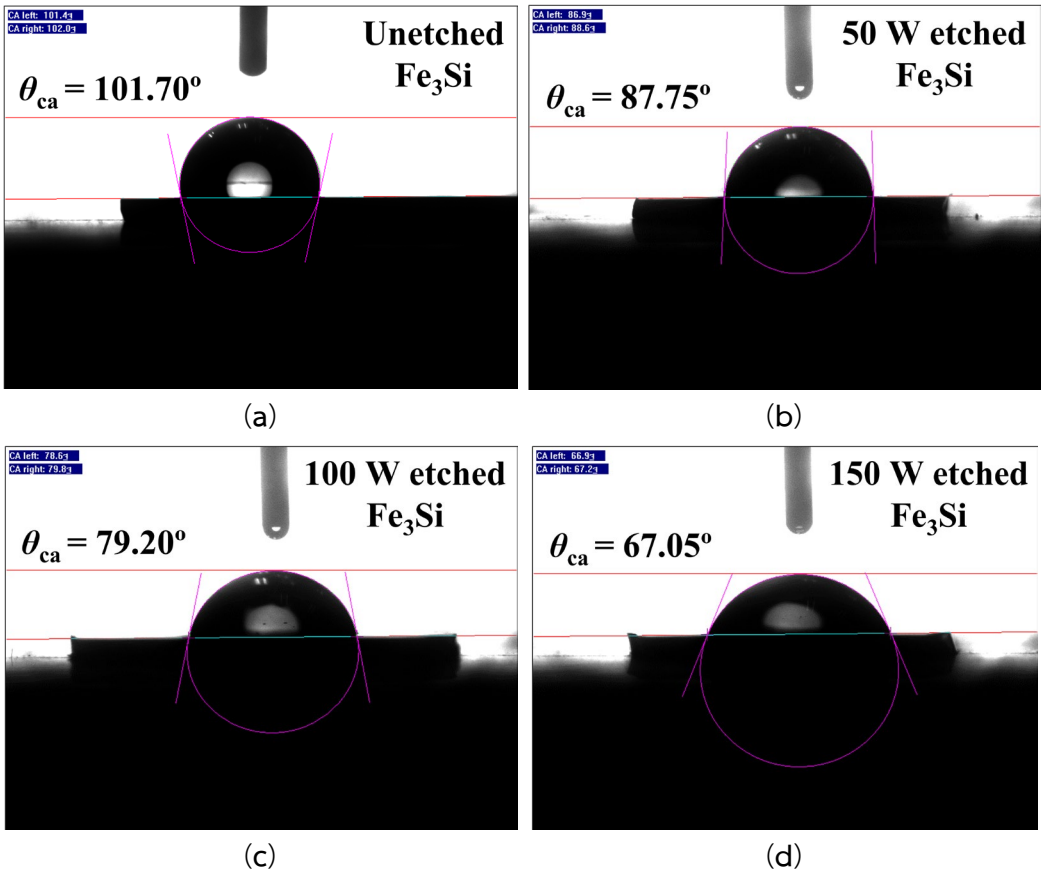

Figure 4.24 Contact angles of (a) as-produced and etched Fe_3Si films at (b) 50, (c) 100, and (c) 150 W.

4.4.6 Mechanical property of unetched and etched Fe_3Si films

Figure 4.25 presents the plot set of the applied indentation load versus the depth of penetration (load–depth curve) for the Fe_3Si films under the conditions of untreated, 50 W treated, 100 W treated, and 150 W treated, respectively. The measurements of etched films were performed in the similar parameter as the unetched films. The H results in Table 4.8 shows the decreasing trend of the hardness characteristic of Fe_3Si films with increasing Ar plasma treatment power. In

the same vein, the E_r decreases. Based on the nanoindentation result, the H of the untreated Fe_3Si films was close to the Fe_3Si reported by various sources [78,79]. The standard of H and Er also unnoticeably change as the power increased. The behaviors observed here indicative that plasma etching rarely effect Fe_3Si films.

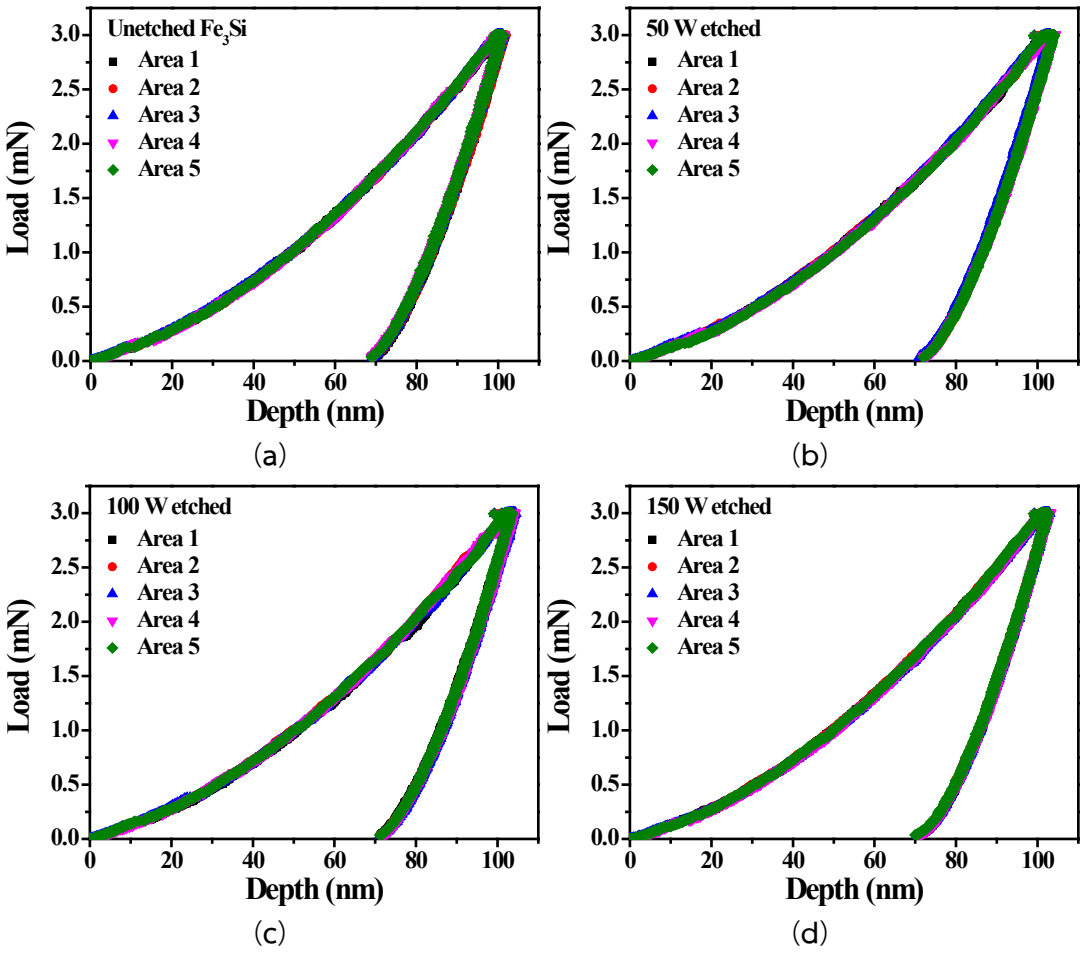

Figure 4.25 Load-depth plots of the as-created Fe_3Si films and the films after etching at 50, 100, and 150 W.

Table 4.8 H and E_r for unetched Fe_3Si and Ar plasma etched Fe_3Si.

Sample	H (GPa)	E_r (GPa)
Unetched Fe_3Si	9.392 ± 0.070	204.862 ± 1.226
Ar etched (50 W; 10 min)	8.991 ± 0.069	205.943 ± 4.633
Ar etched (100 W; 10 min)	8.881 ± 0.080	208.085 ± 3.113
Ar etched (150 W; 10 min)	8.857 ± 0.094	212.693 ± 3.211

Chapter 5
Summary and Suggestions for Future Work

This chapter highlights the experimental data obtained from the research and makes recommendations for future relevant research activity.

5.1 Summary

In this research, nanocrystalline $FeSi_2$ films were epitaxially produced on Si(111) wafer substrates through the utilization of FTDCS. The sputtering pressure was set at 1.33×10^{-1} Pa at room temperature. After production, the as-produced nanocrystalline $FeSi_2$ films were moved to the microwave plasma apparatus and etched for 10 minutes in Ar atmosphere at 50, 100 and 150 W. The XRD results of the as-created nanocrystalline $FeSi_2$ show a broad peak at 2θ ranging from 40 to 50°. The nanocrystalline $FeSi_2$ films etched at 50 to 150 W comprised several preferred orientations evidencing the improved crystallinity. the XPS spectrum revealed that the surface of the untreated Fe_3Si was laden with carbon and oxygen. The Ar plasma etching increasingly reduced the carbon concentration as the power increased by the volatilization of the carbon atoms through ion collision. The rising plasma also increased the presence of radical reactive site which formed into an oxide layer on the nanocrystalline $FeSi_2$ surface. FESEM images of the as-formed nanocrystalline $FeSi_2$ films films exhibits a large amount of crystallites with diameters of less than 5 nm. At an etching power of 50 W, the small pores began to appear within uniform crystallites and became more apparent as the power increased. The R_{rms} of the as-produced nanocrystalline $FeSi_2$ films was 1.04 Å, which changed slightly after etching. The θ_{ca} between the water droplet and as-produced nanocrystalline $FeSi_2$ film surface was 100.55°, showing that the surface of the nanocrystalline $FeSi_2$ films was hydrophobic. The θ_{ca} value reduced to 53.90°, 43.60°, and 35.65° at an etching power of 50, 100, and 150 W. The change in wettability of the nanocrystalline $FeSi_2$ films from hydrophobic to hydrophilic was mainly dictated by chemical alteration after plasma etching. Nanoindentation revealed H value of 9.616 GPa and E_r value of 159.146 GPa for the unetched. After etching with Ar plasma, the value of H and E_r remained relatively unchanged.

Utilizing FTDCS, Fe_3Si films were created at temperature of 300 °C. The Fe_3Si films were etched using power of 50, 100, and 150 W under Ar gas for 10minutes. The XRD results of the as-created Fe_3Si show multiple peaks of Fe_3Si representing a combination of a B_2 and DO_3 crystal structure. The Fe_3Si films etched at 50 and 100 W showed gradual improved crystallinity, while 150 W Ar plasma may cause a slight damage to the surface structure. the XPS spectrum of Fe_3Si films yielded similar trend to that of nanocrystalline $FeSi_2$ but with noticeable higher oxide concentration. Based on FESEM micrographs in planar view, the unetched Fe_3Si films were composed of a large amount of small uniform crystallites, which became more porous as the plasma etching power increased. From an AFM micrograph, the unetched Fe_3Si films showed a very smooth surface with a R_{rms} of 10.63 Å, which was increased by etching. The unetched Fe_3Si films exhibited an θ_{ca} of 101.7°, indicating hydrophobic properties. After plasma etching, the film surface turned to hydrophilic surface with lowest contact angle of 67.05° at 150 W. The H and E_r of the Fe_3Si films were not significantly influenced by the Ar plasma at different powers. The findings of the experiments showed that the etching power had an effect on the surface morphology, as well as the structural, chemical composition, and wettability properties of both nanocrystalline $FeSi_2$ and Fe_3Si films without compromising mechanical qualities.

5.2 Suggestions

The current study offers the following recommendations for further relevant investigation:

1) The surface morphology and wettability of the nanocrystalline $FeSi_2$ and Fe_3Si films should be studied under different etching atmospheres, such as O_2, N_2, and CF_4.
2) The surface morphology and wettability of the nanocrystalline $FeSi_2$ and Fe_3Si films should be studied with different etching times, pressure, and flow rate.
3) The aging effect on the nanocrystalline $FeSi_2$ and Fe_3Si films after plasma etching should be studied.
4) Plasma profile should be observed through optical emission spectroscopy.
5) Wear resistance should be tested along with other mechanical properties.

References

[1] Promros, N., Yamashita, K., Iwasaki, R., and Yoshitake, T. 2012. “Effects of Hydrogen Passivation on Near-Infrared Photodetection of n-Type β-$FeSi_2$/p-Type Si Heterojunction Photodiodes.”, Jpn. J. Appl. Phys. 51 : 108006.

[2] Shaban, M., Nakashima, K., Yokoyama, W., and Yoshitake, T. 2007. “Photovoltaic Properties of n-Type β-$FeSi_2$/p-Type Si Heterojunctions.”, Jpn. J. Appl. Phys. 46 : L667.

[3] Nakagauchi, D., Yoshitake, T., and Nagayama, K. 2004. “Fabrication of Ferromagnetic Fe_3Si Thin Films by Pulsed Laser Deposition Using an Fe_3Si Target.”, Vacuum. 74 : 653–657.

[4] Yoshitake, T., Nakagauchi, D., Ogawa, T., Itakura, M., Kuwano, N., Tomokiyo, Y., Kajiwara T., and Nagayama, K. 2004. “Room-Temperature Epitaxial Growth of Ferromagnetic Fe_3Si Films on Si(111) by Facing Target Direct-Current Sputtering.”, Appl. Phys. Lett. 86 : 262505.

[5] Sadoh, T., Takeuchi, H., Ueda, K., Kenjo, A., and Miyao, M. 2006. “Epitaxial Growth of Ferromagnetic Silicide Fe_3Si on Si(111) Substrate.”, Jpn. J. Appl. Phys. 45 : 3598.

[6] Schneeweiss, O., Pizurova, N., Jiraskova, Y., Žák, T., and Cornut, B. 2000. “Fe_3Si Surface Coating on SiFe Steel.”, J. Magn. Magn. Mater. 215 : 115–117.

[7] Promros, N., Yamashita, K., Izumi, S., Iwasaki, R., Shaban, M., and Yoshitake, T. 2012. “Near-infrared photodetection of *n*-type β-$FeSi_2$/intrinsic Si/*p*-type Si heterojunctions at low temperatures.”, Jpn. J. Appl. Phys. 51 : 09MF02.

[8] Chaleawpong, R., Promros, N., Charoenyuenyao, P., Nopparuchikun, A., Sittimart, P., Nogami, T., and Yoshitake, T. 2018. “Production of *p*-type Si/*n*-type β-$FeSi_2$ heterojunctions using facing-targets direct-current sputtering and evaluation of their resistance and interface state density.”, Phys. Status Solidi A 215 : 1701022.

[9] Milosavljević, M., Shao, G., Bibić, N., McKinty, C. N., Jeynes, C., and Homewood, K. P. 2001. “Amorphous-iron disilicide: A promising semiconductor.”, Appl. Phys. Lett. 79 : 1438-1440.

[10] Milosavljević, M., Shao, G., Lourenço, M. A., Gwilliam, R. M., Homewood, K. P., Edwards, S. P., Valizadeh, R., and Colligon, J. S. 2005. “Transition from amorphous to crystalline beta phase in co-sputtered $FeSi_2$ films as a function of temperature.”, J. Appl. Phys. 98 : 123506.

[11] Promros, N., Yamashita, K., Li, C., Kawai, K., Shaban, M., Okajima, T., and Yoshitake, T. 2012. *“n*-Type nanocrystalline $FeSi_2$/intrinsic Si/*p*-type Si heterojunction photodiodes fabricated by facing-target direct-current sputtering.”, Jpn. J. Appl. Phys. 51 : 021301.

[12] Charoenyuenyao, P., Promros, N., Chaleawpong, R., Borwornpornmetee, N., Sittisart, P., Tanaka, Y., and Yoshitake, T. 2020. “Wettability, Morphological and Wetting Properties of Semiconducting Beta and Nanocrystalline Iron Disilicide Formed via Radio Frequency Magnetron Sputtering.”, Thin Solid Films 709 : 138248.

[13] Charoenyuenyao, P., Promros, N., Chaleawpong, R., Saekow, B., Porntheeraphat, S., and Yoshitake, T. 2019. “Effect of Annealing on Surface Morphology and Wettability of NC-$FeSi_2$ Films Produced via Facing-Target Direct-Current Sputtering.”, J. Nanosci. Nanotechnol. 1 9 : 6834-6840.

[14] Charoenyuenyao, P., Promros, N., Chaleawpong, R., Borwornpornmetee, N., Sittisart, P., Tanaka, Y., and Yoshitake, T. 2020. “Impact of annealing temperature and carbon doping on the wetting and surface morphology of semiconducting iron disilicide formed via radio frequency magnetron sputtering.”, Thin Solid Films 709 : 138248.

[15] Berman, D. and Krim, J. 2012. “Impact of Oxygen and Argon Plasma Exposure on the Roughness of Gold Film Surfaces.”, Thin Solid Films 520 : 6201–6206.

[16] Ujino, D., Nishizaki, H., Higuchi, S., Komasa, S., and Okazaki, J. 2019. “Effect of Plasma Treatment of Titanium Surface on Biocompatibility.”, Appl. Sci. 9 : 2257.

[17] Pransilp, P., Kiatkamjornwong, S., Bhanthumnavin, W., and Paosawatyanyong, B. 2012. “Plasma Nano-Modification of Poly (Ethylene Terephthalate) Fabric for Pigment Adhesion Enhancement.”, J. Nanosci. Nanotechnol. 12 : 481–488.

[18] Taweesub, K., Visuttipitukul, P., Tungkasmita, S., and Paosawatyanyong, B. 2010. “Nitridation of Al–6%Cu Alloy by RF Plasma Process.” Surf. Coat. Technol. 204 : 3091–3095.

[19] Surdu-Bob, C.C., Sullivan, J.L., Saied, S.O., Layberry, R., and Aflori, M. 2012. “Surface Compositional Changes in GaAs Subjected to Argon Plasma Treatment.” Appl. Surf. Sci. 202 : 183–198.

[20] Prysiazhnyi, V., Slavicek, P., Mikmekova, E., and Klima, M. 2016. “Influence of Chemical Precleaning on the Plasma Treatment Efficiency of Aluminum by RF Plasma Pencil.” Plasma Sci. Technol. 18 : 430–437.

[21] Ruand, L. and Jie-Rong, C. 2006. “Studies on Wettability of Medical Poly (Vinyl Chloride) by Remote Argon Plasma.” Appl. Surf. Sci. 252 : 5076–5082.

[22] Borisenko, V.E. 2013. Semiconducting Silicides: Basics, Formation, Properties. Berlin : Springer Science & Business Media.

[23] Chen, L.J. 2004. Silicide Technology for Intregrated Circuits, The institution of London : Engineering and Technology.

[24] Mahan, J.E., Thanh, V.L., Chevrier, J., Berbezier, I., Derrien, J., and Long, R.G. 1993. “Surface electron-diffraction patterns of β-$FeSi_2$ films epitaxially grown on silicon.”, J. Appl. Phys. 74 : 1747-1761.

[25] Bost, M.C. and Mahan, J.E. 1985. “Optical properties of semiconducting iron disilicide thin films.”, J. Appl. Phys. 58 : 2696-2703.

[26] Shaban, M., Nomoto, K., Nakashima, K., and Yoshitake, T. 2008. “Low-temperature annealing of n-type β-$FeSi_2$/p-type Si heterojunctions.”, Jpn. J. Appl. Phys. 47 : 3444-3446.

[27] Christensen, N.E. 1990. “Electronic structure of β-$FeSi_2$.”, Phys. Rev. B. 42 : 7148-7153.

[28] Shaban, M., Nakashima, K., and Yoshitake, T. 2007. “Substrate temperature dependence of photovoltaic properties of β-$FeSi_2$/Si heterojunctions prepared by facing-target DC sputtering.”, Jpn. J. Appl. Phys. 46 : 7708-7710.

[29] Suzuno, M., Koizumi, T., and Suemasu, T. 2009. “p-Si/ β-$FeSi_2$/n-Si double-heterostructure light-emitting diodes achieving 1.6 μm electroluminescence of 0.4 mW at room temperature.”, Appl. Phys. Lett. 94 : 213509.

[30] Gay, J.M., Stocker, P., and Rethore, F. 1993. “X-ray scattering studies of $FeSi_2$ films epitaxially grown on Si (111).”, J. Appl. Phys. 73 : 8169-8178.

[31] Li, X.N., Li, S.B., Nie, L.F., Li, H., Dong, C., and Jiang, X. 2010. “Preparation of amorphous $Fe_xSi_{(1-x)}$ film using unbalanced magnetron sputtering.”, Thin Solid Films 518 : 7390-7393.

[32] Yoshitake, T., Yatabe, M., Itakura, M., Kuwano, N., Tomokiyo, Y., and Nagayama, K. 2003. “Semiconducting nanocrystalline iron disilicide thin films prepared by pulsed-laser ablation.”, Appl. Phys. Lett. 83 : 3057-3059.

[33] Milosavljević, M., Wong, L., Lourenço, M., Valizadeh, R., Colligon, J. Sha, G., and Homewood, K.P. 2010. “Correlation of structural and optical properties of sputtered $FeSi_2$ thin films.”, Jpn. J Appl. Phys. 49 : 081401.

[34] Shaban, M., Kondo, H., Nakashima, K., and Yoshitake, T. 2008. “Electrical and photovoltaic properties of n-type nanocrystalline-$FeSi_2$/p-type Si heterojunctions prepared by facing-targets direct-current sputtering at room temperature.”, Jpn. J. Appl. Phys. 47 : 5420-5422.

[35] Takarabe, K., Doi, H., Mori, Y., Fukui, K., Shim, Y., Yamamoto, N., Yoshitake, T., and Nagayama, K. 2006. “Optical properties of nanocrystalline $FeSi_2$ and the effects of hydrogenation.”, Appl. Phys. Lett. 88 : 061911.

[36] Shaban, M., Kawai, K., Promros, N., and Yoshitake, T., 2010. “n-Type nanocrystalline-$FeSi_2$/p-Type Si heterojunction photodiodes prepared at room temperature.”, IEEE Electron Device Lett. 31 : 1428-1430.

[37] Nakamura, S., Aoki, T., Kittaka, T., Hakamata, R., Tabuchi, H., Kunitsugu, S., and Takarabe, K.I. 2007. “Facing target sputtered iron-silicide thin film.”, Thin Solid Films 515 : 8205-8209.

[38] Starke, U., Schardt, J., Weiss, W., Meier, W., Polop, C., De Andres, P. L., and Heinz, K. 2001. “Structural and compositional reversible phase transitions on low-index Fe3Si surfaces.”, EPL 56 : 822.

[39] Zhang, Y., and Ivey, D. G. 1998. “Fe_3Si formation in Fe–Si diffusion couples.”, J. Mater. Sci. 33 : 3131-3135.

[40] Hamaya, K., Ueda, K., Kishi, Y., Ando, Y., Sadoh, T., and Miyao, M. 2008. “Epitaxial ferromagnetic Fe_3Si/Si (111) structures with high-quality heterointerfaces”, Appl. Phys. Lett. 93 : 132117.

[41] Herfort, J., Schönherr, H. P., and Ploog, K. H. 2003. “Epitaxial growth of Fe_3Si/GaAs (001) hybrid structures.”, Appl. Phys. Lett. 83 : 3912-3914.

[42] Yakovlev, I. A., Varnakov, S. N., Belyaev, B. A. E., Zharkov, S. M., Molokeev, M. S., Tarasov, I. A. E., and Ovchinnikov, S. G. E. 2014. “Study of the structural and magnetic characteristics of epitaxial Fe_3Si/Si (111) films”, JETP letters. 99 : 527-530.

[43] Wasa, K., and Hayakawa, S. 1992. Handbook of Sputter Deposition Technology: Principles, Technology, and Applications. New Jersey : Noyes Publication.

[44] Kadokura, S. Facing-targets-type sputtering apparatus and method. U.S. patent no. 6911123B2. June 2005.

[45] Kadokura, S. Facing Target Type Sputtering Apparatus. U.S. patent no. 6156172. December 2000.

[46] Yoshikawa, T. Facing Targets Sputtering Device. U.S. patent no. 5000834. March 1991.

[47] Flamma, D. L., and Herb G. K. 1989. Plasma Etching || Plasma Etching Technology—An Overview. Amsterdam : Elsevier.

[48] Harry, J. E. 2013. Introduction to plasma technology: science, engineering, and applications. New Jersey : John Wiley & Sons.

[49] Yuan, Y. and Lee, T.R. 2013. Surface Science Techniques. Berlin : Springer-Verlag Berlin Heidelberg.

[50] Schrader, M.E. and Loeb, G.I. 2013. Modern approaches to wettability: theory and applications. Maryland, Springer Science & Business Media.

[51] Mohamed, A.M., Abdullah, A.M., and Younan, N.A. 2015. “Corrosion behavior of superhydrophobic surfaces: A review.” Arab. J. Chem. 8: 749-765.

[52] Bormashenko, E. 2015. “Progress in understanding wetting transitions on rough surfaces.” Adv. Colloid Interface Sci. 222 : 92-103.

[53] Wenzel, R.N. 1936. “Resistance of solid surfaces to wetting by water.” Industrial & Engineering Chemistry. 28(8) : 988-994.

[54] Cassie, A.B.D. and Baxter, S. 1944. “Wettability of porous surfaces.” Transactions of the Faraday society. 40 : 546-551.

[55] Bunaciu, A.A., Udriştioiu, E.G., and Aboul-Enein, H.Y. 2015. “X-ray diffraction: instrumentation and applications.”, Crit. Rev. Anal. Chem. 45 : 289-299.

[56] Prysiazhnyi, V. 2012. Atmospheric pressure plasma treatment of metal surfaces by DCSBD plasma source: effects of plasma treatment and aging effect of plasma treated surfaces. Brno : Masaryk University.

[57] Joy, D.C., Bradbury, S. and Ford, B.J. 2019. Scanning electron microscope. [Online]. Available : https://www.britannica.com/technology/scanning electron-microscope.

[58] Zeng, C., Vitale-Sullivan, C. and Ma, X. 2017. “In situ atomic force microscopy studies on nucleation and self-assembly of biogenic and bio-inspired materials.”, Minerals 7 : 158.

[59] Mendes, B. 2020. Functionalization of Silicon Carbide (SiC) for Abrasive Filament Production. Lisbon : Instituto Superior Técnico.

[60] Sun, X., Li, L., Guo, Y., Zhao, H., Zhang, S., Yu, Y., Wu, D., Liu, H., Yu, M., Shi, D., Liu, Z., Zhou, M., Ren, L. and Fu, L. 2018. “Influences of organic component on mechanical property of cortical bone with different water content by nanoindentation.”, AIP Advances 8 : 035003.

[61] Muthitamongkol, P., Thanachayanont, C., Samransuksamer, B., Seawsakul, K., Horprathum, M., Eiamchai, P., Limwichean, S., Patthanasettakul, V., Nuntawong, N., Songsiriritthiguland, P., and Chindaudom, P. 2017. "The effects of the argon plasma treatments on transparent conductive aluminum-dope zinc oxide thin films prepared by the pulsed DC magnetron sputtering.", Mater. Today: Proc. 4 : 6248–6253.

[62] Zaien, M., Ahme, N.M., and Hassan, Z. 2013. "Effects of annealing on the optical and electrical properties of CdO thin films prepared by thermal evaporation.", Materials Letters. 105 : 84-86.

[63] Liu, C., Yuan, Y., Jiang, J.T., Gong, Y.X., and Zhen, L. 2015. "Microwave absorption properties of FeSi flaky particles prepared via a ball-milling process.", Journal of Magnetism and Magnetic Materials. 395 : 152-158.

[64] Chen, G.L., Peng, J.H., and Xu, W.X. 1998. "Surface Reaction of Polycrystalline Fe_3Si Alloys with Oxygen and Water Vapor.", Intermetallics 6 : 315–322.

[65] Calaway, M.J. and Fries, M.D. "Adventitious Carbon on Primary Sample Containment Metal Surfaces." In Proceedings of the 46th Lunar and Planetary Science Conference, The Woodlands Waterway Marriott Hotel and Convention Center, The Woodlands, TX, USA, 16–20 March 2015 : p. 1517.

[66] Fischer-Cripps, A.C. 2000. "A Review of Analysis Methods for Sub-Micron Indentation Testing.", Vacuum 58 : 569–585.

[67] Lu, C.J. and Bogy, D.B. 1995. "The Effect of Tip Radius on Nano-Indentation Hardness Tests.", Int. J. Solids Struct. 32 : 1759–1770.

[68] Oliver, W.C. and Pharr, G.M. 1992. "An Improved Technique for Determining Hardness and Elastic Modulus Using Load and Displacement Sensing Indentation Experiments.", J. Mater. Res. 7 : 1564–1583.

[69] Beegan, D., Chowdhury, S., and Laugier, M.T. 2007. "Comparison between Nanoindentation and Scratch Test Hardness (Scratch Hardness) Values of Copper Thin Films on Oxidised Silicon Substrates.", Surf. Coat. Technol. 201 : 5804–5808.

[70] Charoenyuenyao, P., Promros, N., Chaleawpong, R., Saekow, B., Porntheeraphat, S., and Yoshitake, T. 2020. “Influence of annealing temperature on mechanical and wetting properties of β-$FeSi_2$ films built using facing-targets direct-current sputtering.” J. Nanosci. Nanotechnol. 20 ; 621-628.

[71] Wei, Q., Sharma, A. K., Sankar, J., and Narayan, J. 1999. “Mechanical properties of diamond-like carbon composite thin films prepared by pulsed laser deposition.” Compos. B. Eng. 30 ; 675-684.

[72] Savvides, N., and Bell, T. J. 1993. “Hardness and elastic modulus of diamond and diamond-like carbon films.” Thin Solid Films 228 ; 289-292.

[73] Sattar, H., Jielin, S., Ran, H., Imran, M., Ding, W., Gupta, P.D., and Ding, H. 2020. “Impact of Microstructural Properties on Hardness of Tungsten Heavy Alloy Evaluated by Stand-Off LIBS after PSI Plasma Irradiation.”, J. Nucl. Mater. 540 : 152389.

[74] Fernández, S., Santos, J.D., Munuera, C., García-Hernández, M., and Naranjo, F.B. 2015. “Effect of Argon Plasma-Treated Polyethylene Terepthalate on ZnO:Al Properties for Flexible Thin Film Silicon Solar Cells Applications.”, Sol. Energy Mater. Sol. Cells 133 : 170–179.

[75] Chen, L., Ahadi, A., Zhou, J., and Ståhl, J.-E. 2013. “Modeling Effect of Surface Roughness on Nanoindentation Tests.” Procedia CIRP 8 : 334–339.

[76] Hirakawa, S.I., Sonoda, T., Sakai, K.I., Takeda, K., and Yoshitake, T. 2011. “Temperature-Dependent Current-Induced Magnetization Switching in $Fe_3Si/FeSi_2/Fe_3Si$ Trilayered Films.”, Jpn. J. Appl. Phys. 50 : 08JD06.

[77] Tang, C.B., Wen, F.R., Chen, H.X., Liu, J.J., Tao, G.Y., Xu, N.J., and Xue, 2019. “J.Q. Corrosion Characteristics of Fe_3Si Intermetallic Coatings Prepared by Molten Salt Infiltration in Sulfuric Acid Solution.”, J. Alloys Compd. 778 : 972–981.

[78] Murakami, T., Hibi, Y., Mano, H., Matsuzaki, K., and Inui, H. 2012. “Friction and Wear Properties of Fe-Si Intermetallic Compounds in Ethyl Alcohol.”, Intermetallics 20 : 68–75.

[79] Odrobina, I., Kúdela, J., and Kando, M. 1998. “Characteristics of the Planar Plasma Source Sustained by Microwave Power.”, Plasma Sources Sci. Technol. 7 : 238.

Appendix/Appendices

Appendix A

Supplementary Materials for Magnetic Properties

Vibrating sample magnetometer (VSM) of unetched and etched Fe_3Si films were measured through custom-made VSM based on Lake Shore, model 730908 at room temperature with maximum applied magnetic field of 3 kOe. The result reveals saturated magnetization of the constructed Fe3Si films to be 1.318×10^{-2} emu/g. After plasma treated, the films show an unclear trend of magnetization of 2.571×10^{-2} emu/g, 1.522×10^{-2} emu/g, and 1.774×10^{-2} emu/g for 50 W, 100 W, and 150 W treated films. The VSM plot between mass magnetization versus applied magnetic field reveals an unclear trend of results, as depicted in Figure S1(a). This result probably originated from an error of instrument and film inconsistency rather than the effect of Ar plasma treatment, as evident by the identical hysteresis loops of each Fe_3Si film shown in Figure S1(b).

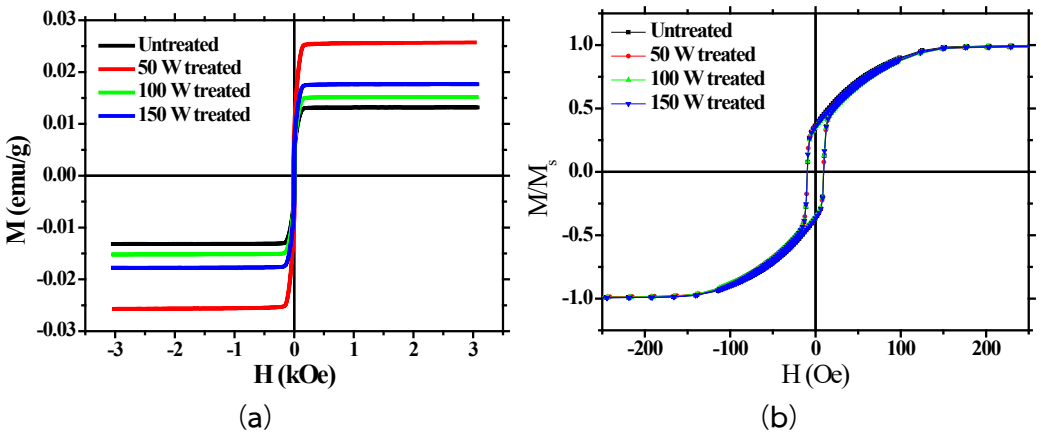

Figure S1. The (a) VSM plot between mass magnetization versus applied magnetic field and (b) hysteresis loop of the etched and unetched Fe_3Si film's surface

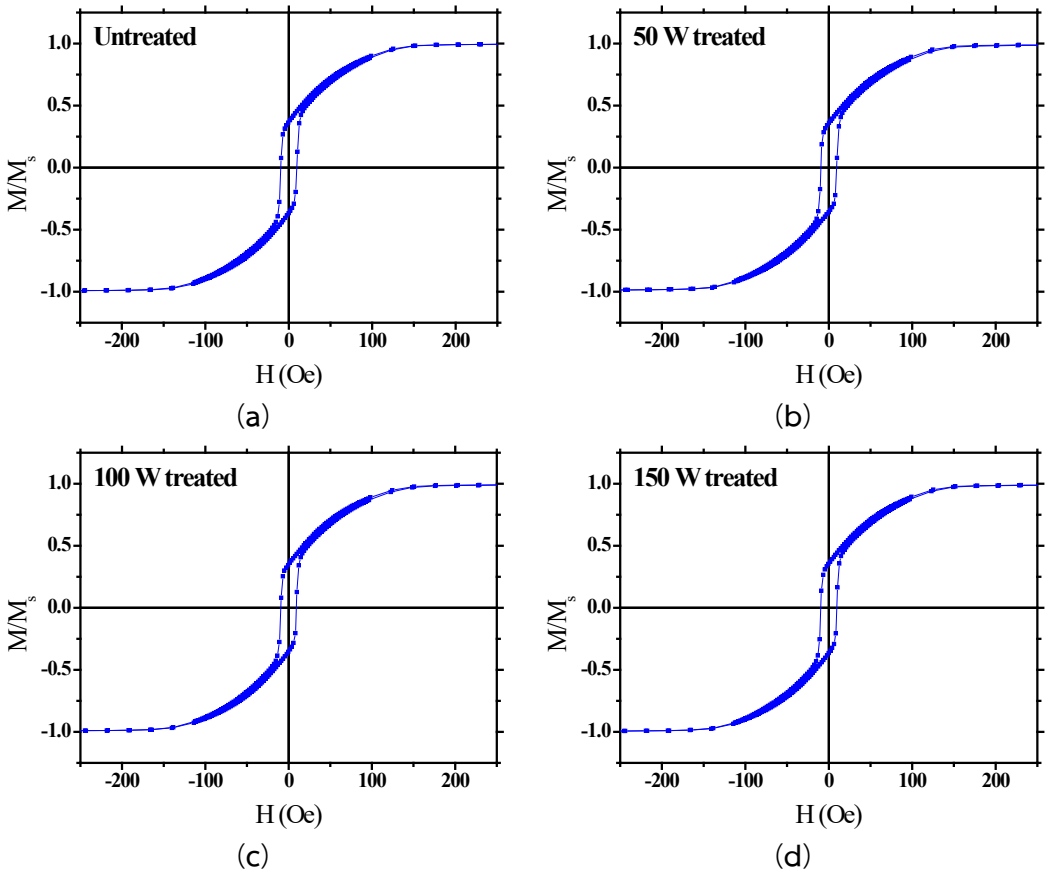

Figure S2. The separated hysteresis loop based on plot between ratio of mass magnetization and saturated magnetization versus applied magnetic field of (a) unetched, (b) 50 W, (c) 100 W and (d) 150 W treated Fe_3Si film.

Author Biography

Name	Mr.Nattakorn Borwornpornmetee	
Date of Birth	12 January 1997	
Education	2018 Bachelor of Science in Physics	GPA 2.88
	King Mongkut's Institute of Technology Ladkrabang	
	2022 Major of Science in Physics	GPA 3.75
	King Mongkut's Institute of Technology Ladkrabang	

Experiences and Achievements

- KMITL Doctoral Scholarship: 2022
- Teaching assistant on MiniTab and DOE lab of Atomic Structure and Solid State Physics Laboratory, academic year 2020
- Research Assistant and Teaching Assistant Scholarship: 2019
- International research internship at Kyushu University: Jan-Feb, 2019

Awards

Years	Awards	Organizations
2022	Best presentation "Design and Characterization of Surface Dielectric Barrier Discharge Plasma System"	The 5th CRU-National Conference in Science and Technology Bangkok, Thailand, 16 June, 2022.
2022	First Place (Social Science, Humanity, and Management Group) "Warehouse Management"	KMITL Cooperative Education Exhibition 2021 Bangkok, Thailand, Jan 25, 2022
2022	First Place (Science and Technology Group) "Study and Improvement Epoxy Resin Bleed at Die Attach Operation for IC Copper Clip Package"	KMITL Cooperative Education Exhibition 2021 Bangkok, Thailand, Jan 25, 2022

2021	Silver Medal "Design and Construct of Air Purifier for Hospital Use"	Thailand Research Expo 2021 Bangkok, Thailand, June 27- July 1, 2021
2020	Best Poster Award "Nitrogen Plasma Etching of Indium Tin Oxide Nanorod Film Surface at Different Radio-Frequency Powers"	The 6th International Conference on Electronic Materials and Nanotechnology for Green Environment: **ENGE 2020** Ramada Plaza Jeju Hotel, Jeju, Korea, November 1-4, 2020
2019	Best Poster Award "Wetting, Structural and Surface Morphological Properties of C-doped β-$FeSi_2$ Thin Films Prepared via Radio-Frequency Magnetron Sputtering"	The 5th International Conference on Advanced Electromaterials: **ICAE 2019** Ramada Plaza Jeju Hotel, Jeju, Korea, November 5-8, 2019

Academic Publications

1. **Nattakorn Borwornpornmetee**, Rawiwan Chaleawpong, Peerasil Charoenyuenyao, Adison Nopparuchikun, Boonchoat Paosawatyanyong, Phongsaphak Sittimart, Tsuyoshi Yoshitake, Nathaporn Promros, Reverse Bias Dependent Impedance and Dielectric Properties of Al/*n*-NC $FeSi_2$/*p*-Si/Pd Heterostructures Formed by Facing-Targets Sputtering, Materials Science in Semiconductor Processing Vol. 146 (2022) Article No. 106641. (Impact factor 4.644, Q1) Indexed in Web of science.
2. Peerasil Charoenyuenyao, Rawiwan Chaleawpong, **Nattakorn Borwornpornmetee**, Boonchoat Paosawatyanyong, Phongsaphak Sittimart, Tsuyoshi Yoshitake, Nathaporn Promros, Investigation of Morphological Surface Features, Wetting Behavior and Mechanical Traits under Various Substrate Temperatures for Beta Iron Disilicide Prepared via Facing-Targets Sputtering, Materials Science in Semiconductor Processing Vol. 146 (2022) Article No. 106604 (Impact factor 4.644, Q1) Indexed in Web of science.
3. **Nattakorn Borwornpornmetee**, Peerasil Charoenyuenyao, Rawiwan

Chaleawpong, Boonchoat Paosawatyanyong, Rungrueang Phatthanakun, Phongsaphak Sittimart, Kazuki Aramaki, Takeru Hamasaki, Tsuyoshi Yoshitake, Nathaporn Promros, Physical Properties of Fe_3Si Films Coated through Facing Targets Sputtering after Microwave Plasma Treatment, Coatings Vol. 11 (2021) Article No. 923. (Impact factor 3.236, Q2) Indexed in Web of science.

4. Rawiwan Chaleawpong, Nathaporn Promros, Peerasil Charoenyuenyao, Phongsaphak Sittimart, Pattarapol Sittisart, **Nattakorn Borwornpornmetee**, Yuki Tanaka, Tsuyoshi Yoshitake, Photovoltaic, Capacitance-Voltage, Conductance-Voltage, and Electrical Impedance Characteristics of p-Type Silicon/Intrinsic-Silicon/n-Type Semiconducting Iron Disilicide Heterostructures Built via Facing Target Direct-Current Sputtering, Thin Solid Films, Vol. 709 (2020) Article No. 138229. (Impact factor 2.183, Q3) Indexed in Web of science.
5. Peerasil Charoenyuenyao, Nathaporn Promros, Rawiwan Chaleawpong, **Nattakorn Borwornpornmetee**, Pattarapol Sittisart, Yuki Tanaka, Tsuyoshi Yoshitake, Wettability, Morphological and Wetting Properties of Semiconducting Beta and Nanocrystalline Iron Disilicide Formed via Radio Frequency Magnetron Sputtering, Thin Solid Films, Vol. 709 (2020) Article No. 138248. (Impact factor 2.183, Q3) Indexed in Web of science.
6. Peerasil Charoenyuenyao, Nathaporn Promros, Rawiwan Chaleawpong, Pitoon Noymaliwan, **Nattakorn Borwornpornmetee**, Surachart Kamoldilok, Supanit Porntheeraphat, Bunpot Saekow, Tanapoj Chaikeeree, Benjarong Samransuksamer, Peerapong Nuchuay, Chanunthorn Chananonnawathorn, Saksorn Limwichean, Mati Horprathum, Pitak Eiamchai, Viyapol Patthanasettakul, Influence of an Annealing Temperature in a Vacuum Atmosphere on the Physical Properties of Indium Tin Oxide Nanorod Films, Journal of Nanoscience and Nanotechnology, Vol. 20 (2020) 5006-5013. (Impact factor 1.134, Q4) Indexed in Web of science.
7. Peerasil Charoenyuenyao, Nathaporn Promros, Rawiwan Chaleawpong, **Nattakorn Borwornpornmetee**, Pattarapol Sittisart, Yuki Tanaka, Tsuyoshi Yoshitake, Wettability, Surface Morphology and Structural Properties of β-$FeSi_2$ Films Manufactured through Usage of Radio-Frequency Magnetron Sputtering, Journal of Nanoscience and Nanotechnology, Vol. 20 (2020) 5075-5081. (Impact factor 1.134, Q4) Indexed in Web of science.

8. Pattarapol Sittisart, Nathaporn Promros, Rawiwan Chaleawpong, Peerasil Charoenyuenyao, **Nattakorn Borwornpornmetee**, Yuki Tanaka, Tsuyoshi Yoshitake, Light Detection and Carrier Transportation Mechanism in p-Type Si/n-Type Nanocrystalline $FeSi_2$ Heterojunctions produced via Radio-Frequency Magnetron Sputtering, Journal of Nanoscience and Nanotechnology, Vol. 20 (2020) 5082-5088. (Impact factor 1.134, Q4) Indexed in Web of science.